RESEARCH ARTICLE
SPACE PHYSICS: MAGNETOSPHERIC PHYSICS

Earth and Planetary Physics
8: 133–154, 2024
doi: 10.26464/epp2023064

Using restored two-dimensional X-ray images to reconstruct the three-dimensional magnetopause

RongCong Wang[1,2], JiaQi Wang[1,2], DaLin Li[1*], TianRan Sun[1*], XiaoDong Peng[1], and YiHong Guo[3]

[1]National Space Science Center, Chinese Academy of Sciences, Beijing 100190, China;

[2]University of Chinese Academy of Sciences, Beijing100049, China;

[3]Aerospace Information Research Institute, Chinese Academy of Sciences, Beijing 100094, China

Key Points:

- A new image restoration method is proposed for noisy soft X-ray count maps.
- The images processed by the restoration algorithm reconstruct a more accurate and complete three-dimensional (3-D) magnetopause.
- This method was validated by using 3-D X-ray emissivity cubes obtained from the piecewise parabolic method–magnetohydrodynamic (PPMLR-MHD) model and Soft X-ray Imager-simulated observation data.

Citation: Wang, R. C., Wang, J. Q., Li, D. L., Sun, T. R., Peng, X. D., and Guo, Y. H. (2024). Using restored two-dimensional X-ray images to reconstruct the three-dimensional magnetopause. *Earth Planet. Phys.*, *8*(1), 133–154. http://doi.org/10.26464/epp2023064

Abstract: Astronomical imaging technologies are basic tools for the exploration of the universe, providing basic data for the research of astronomy and space physics. The Soft X-ray Imager (SXI) carried by the Solar wind Magnetosphere Ionosphere Link Explorer (SMILE) aims to capture two-dimensional (2-D) images of the Earth's magnetosheath by using soft X-ray imaging. However, the observed 2-D images are affected by many noise factors, destroying the contained information, which is not conducive to the subsequent reconstruction of the three-dimensional (3-D) structure of the magnetopause. The analysis of SXI-simulated observation images shows that such damage cannot be evaluated with traditional restoration models. This makes it difficult to establish the mapping relationship between SXI-simulated observation images and target images by using mathematical models. We propose an image restoration algorithm for SXI-simulated observation images that can recover large-scale structure information on the magnetosphere. The idea is to train a patch estimator by selecting noise–clean patch pairs with the same distribution through the Classification–Expectation Maximization algorithm to achieve the restoration estimation of the SXI-simulated observation image, whose mapping relationship with the target image is established by the patch estimator. The Classification–Expectation Maximization algorithm is used to select multiple patch clusters with the same distribution and then train different patch estimators so as to improve the accuracy of the estimator. Experimental results showed that our image restoration algorithm is superior to other classical image restoration algorithms in the SXI-simulated observation image restoration task, according to the peak signal-to-noise ratio and structural similarity. The restoration results of SXI-simulated observation images are used in the tangent fitting approach and the computed tomography approach toward magnetospheric reconstruction techniques, significantly improving the reconstruction results. Hence, the proposed technology may be feasible for processing SXI-simulated observation images.

Keywords: Solar wind Magnetosphere Ionosphere Link Explorer (SMILE); soft X-ray imager; magnetopause; image restoration

1. Introduction

Since Röntgen discovered X-rays in 1895, they have been widely used in various fields (Röntgen, 1896; Ewald, 1962). Among them, X-ray detectors and telescopes play a prominent role in astrophysics (Gorenstein, 2010). In 1960, the team led by Riccardo Giacconi used a probe rocket to detect X-ray radiation from outside the solar system for the first time, opening a new area of exploration (Giacconi et al., 1962; Tucker and Giacconi, 1985). X-rays are electromagnetic waves that travel at the speed of light in a vacuum. Because of the blocking effect of the Earth's atmosphere, X-rays from outer space cannot reach the ground. To receive cosmic X-ray signals, a probe must be placed tens of kilometers above the upper atmosphere; the best environment is the orbit around the Earth in space. This has made X-ray astronomy an important area of space science research, with X-rays also known as "invisible" cosmic messengers (Bhardwaj et al., 2007; Branduardi-Raymont et al., 2012).

The periodic changes and short-term violent activities of the solar wind are important driving factors affecting the Earth's space environment. When heavy ions contained in the solar wind collide

First author: R. C. Wang, wangrongcong20@mails.ucas.ac.cn
Correspondence to: D. L. Li, lidalin@nssc.ac.cn
T. R. Sun, trsun@spaceweather.ac.cn
Received 26 APR 2023; Accepted 19 SEP 2023.
First Published online 14 NOV 2023.

with neutral atoms or molecules in the outer space of the Earth, a solar wind charge exchange (SWCX) occurs, resulting in soft X-ray radiation (Lisse et al., 1996; Cravens, 1997; Snowden et al., 2009; Carter et al., 2010). The SWCX offers a new method for remote detection of a large-scale magnetopause: soft X-ray imaging (Walsh et al., 2016; Sibeck et al., 2018). The Solar wind Magnetosphere Ionosphere Link Explorer (SMILE) is a collaborative space science exploration project sponsored by the Chinese Academy of Sciences and the European Space Agency (Branduardi-Raymont et al., 2016; Wang C et al., 2017), which is expected to launch in 2025. The SMILE satellite will be equipped with a telescopic Soft X-ray Imager (SXI) to acquire large-scale images of the magnetopause near the subpolar regions, with a lobster-eye optical system (Collier et al., 2012). The SXI has a large field of view (FOV): 16° × 27° (Peele et al., 2004). The observation data (0.2–5.0 keV soft X-rays) obtained by the SXI, known as two-dimensional (2-D) soft X-ray images, carry much information about the large-scale magnetosheath structure, which is of great significance for studying the changes in the Earth's magnetosheath under the influence of the solar wind.

How to reconstruct a three-dimensional (3-D) magnetopause profile by using 2-D soft X-ray images is an oft-studied problem (Collier et al., 2018; Jorgensen et al., 2019b; Sun TR et al., 2020). The newly proposed computed tomography approach (CTA) can reconstruct the complete magnetopause profile by using 2-D soft X-ray images from different angles and has proved feasible (Jorgensen et al., 2022; Wang RC et al., 2023). The CTA uses the geometric relationship between 2-D soft X-ray images and imaging from different angles to reconstruct a 3-D Earth magnetopause profile through a reconstruction algorithm. Previous studies on CTA methods were based on theoretical clean 2-D soft X-ray images obtained by a magnetohydrodynamic (MHD) model and did not consider the influence of various factors on SXI imaging in actual situations. In practice, the imaging process of the SXI will be affected by many factors, such as the cosmic sky background of soft X-ray bands, the noise of the imaging instruments, and the fluctuation noise (Guo YH et al., 2021, 2022), resulting in the loss of some edge information from the 2-D soft X-ray images and the blurring of structural features, which will bring about difficulties in the reconstruction of the 3-D magnetopause (Wang RC et al., 2023). Therefore, how to extract useful magnetospheric structure information from SXI observation images for the reconstruction of the 3-D magnetopause is both scientific and practical work.

The rapidly changing space environment and the impact of the SXI observation instrument itself will contribute some interference in the magnetospheric observation imaging. Therefore, a problem to be solved is image restoration of the SXI observation images to help the CTA method better reconstruct the 3-D magnetospheric X-ray emissivity profiles (Jorgensen et al., 2019a, 2022; Wang RC et al., 2023). The purpose of image restoration is to recover high-quality images from low-quality observation data, a classic problem in image processing and computer vision (Gu SH and Timofte, 2019). Our research objective is to estimate and recover 2-D soft X-ray images $\boldsymbol{x}$ of the Earth's magnetosheath from different angles through SXI observation data $\boldsymbol{y}$, with the form $\boldsymbol{y} = \boldsymbol{H}\boldsymbol{x} + \boldsymbol{e}$, where $\boldsymbol{x}$ is the unknown high-quality original image (target image); $\boldsymbol{H}$ is the matrix model for the observation or degradation process (e.g., fuzzy, convoluted, projection), which may vary with some variables or may be fixed; $\boldsymbol{y}$ is the observation data; and $\boldsymbol{e}$ is the noise error (Niknejad et al., 2019). The restoration results must retain most of the magnetospheric structure and edge information and eliminate 2-D soft X-ray image discretization and blurring caused by fluctuation noise.

Previous image restoration methods have usually addressed one observation and noise model, and image restoration work has been applied to Gaussian denoising, that is, observation matrix $\boldsymbol{H} = \boldsymbol{I}$ (unit matrix). Some of these methods rely solely on the noisy image itself, without considering clean images (Buades et al., 2005, 2009; Elad and Aharon, 2006; Dabov et al., 2007; Dong WS et al., 2013; Niknejad et al., 2015; Teodoro et al., 2015). However, this causes some limitations to the restoration results. Hence, researchers have considered methods that rely on a clean image dataset (Luo EM et al., 2015) and a dataset of noisy and clean images (Mosseri et al., 2013; Chen F et al., 2015), with excellent results in various classic image restoration tasks. With the development of deep neural networks, deep learning methods have brought rapid development to various fields of computer imaging and vision, including degraded image restoration (Krizhevsky et al., 2012). Deep learning methods for image restoration include full convolutional networks (Shelhamer et al., 2017), autoencoders (Liou et al., 2008, 2014), and generative adversarial networks (GANs; Goodfellow et al., 2014), which learn the mapping relationship between the clean and observed images to train an image estimator whose input is the observed image and output is the clean image. However, these methods require a large number of external datasets as training data, and most such methods require separate training for different image restoration tasks, or even different parameters of the observation model (i.e., noise variance). As a result, datasets must be retrained for different image restoration tasks, which makes for poor self-adaptability. Another image restoration method that relies on some external datasets but does not need large-scale training is able to learn some parameter distributions from image patches based on Gaussian mixture models and regularize the restored image by using the learned models (Zoran and Weiss, 2011). Because this method is limited to the linear inverse problem of Gaussian noise, namely, that it is difficult to obtain the maximum a posteriori or minimum mean square error estimation of other noise models, it achieves good results only in the image restoration task of Gaussian denoising. However, it opens up a new perspective on the study of image restoration methods.

The use of image sample patches based on external datasets (rather than learning parameter models) to restore observed image patches has gradually become an effective image restoration method (Freeman et al., 2002; Hays and Efros, 2007; Adams et al., 2009; Zontak and Irani, 2011; Chan SH et al., 2014). Most such methods calculate a weighted average of the center pixels of a clean image patch (selected from an external dataset) to estimate the center pixels of the target patch. The weight is derived from the exponent of the negative distance between the noisy and clean patches. This idea originates from the internal nonlocal means (I-NLM) filtering method (Buades et al., 2005), which is an improved filtering denoising method among the traditional neighborhood filtering methods. Inspired by the I-NLM, the external nonlocal mean (E-NLM) method (Levin and Nadler, 2011)

selects a similar set of patches from an external dataset to estimate the patch of the observed image, which requires calculating the distance between the patch of the image to be restored and that of the external dataset. Initially, the distance between patches is obtained by dividing the L2 norm of the difference between patches by the noise variance of the observed image patches (Levin et al., 2012), but it does not apply to all image restoration tasks. The similarity and accessibility of various image patches give this method a strong adaptive ability, but large-scale image patch-matching has huge computational costs. Several approaches have addressed this issue by speeding up patch matching (Barnes et al., 2010; He KM and Sun J, 2012). These methods are usually heuristic and rely on some clustering hierarchical approach.

On the basis of the E-NLM, deep learning, and the correlation analysis of the matrix $\boldsymbol{H}$ for observation process modeling in Section 2.3, we propose an image restoration method for SXI observation images that is suitable for large-scale external datasets and observation models that cannot be modeled generally. The method constructs a large-scale patch pair dataset of 2-D soft X-ray images based on the MHD model and SXI observation images. We use classification expectation–maximization (CEM; Celeux and Govaert, 1992) to classify datasets of large-scale patches, and the patch dataset corresponding to each cluster is used to train the patch estimator based on the deep neural network to obtain each cluster estimator. Classification expectation–maximization is used to divide the observation model H into several local observation models h. The idea is similar to polynomial fitting, where several models h can be infinitely approximated to H. This method can improve the training efficiency and accuracy of the estimator and further enhance the generalization of the overall regression method. The patch estimator is used to establish the potential relationship between the SXI-simulated observation image patch and the MHD model 2-D X-ray image patch (i.e., to model the local observation model h). In experimental verification, we split the SXI observation images of the test set into several image patches. According to the CEM algorithm, the patches of these observed images are classified, and the patch estimator trained by each cluster is used to estimate the observed image patches divided into clusters. The estimated patch is returned to the original position in the image, and the pixel values of the overlapping area are averaged. The restored image is smoothed by an adaptive smoothing filter.

The remainder of this article is organized as follows. Section 2 outlines the data used in this work, as used in the experiments presented in Section 4. Section 3 introduces the proposed image restoration method. Section 4 reports the experimental results of SXI-simulated observation image restoration. Section 5 provides concluding remarks and a discussion of future work.

2. Mission Data Introduction

Here, we introduce the X-ray emissions and X-ray intensity techniques for obtaining the 2-D MHD X-ray images and SXI photon count images that are analyzed in Section 2.3.

2.1 X-Ray Emissions

The global MHD code was used to simulate solar wind–magnetosphere interactions, and the piecewise parabolic method–magnetohydrodynamic model (PPMLR-MHD; Hu YQ et al., 2007) was applied to generate 3-D X-ray emissivity data. The code used an extended Lagrangian version of the PPMLR to solve the MHD equation in the solution domain, whose scope is $-300\ R_E \le x \le 30\ R_E$, $-150\ R_E \le y, z \le 150\ R_E$, with a minimum grid spacing of $0.1 R_E$, and the resolution near the subsolar point is 0.4 R_E. The ionosphere was simplified to a spherical shell with uniform Pedersen conductance (5 S in this work) and zero Hall conductance. The influence of dipole tilt was not considered.

During simulation, the solution domain was divided into a grid of size of $M \times N \times L$, where M, N, and L are the numbers of grids in the X, Y, and Z directions, respectively. The method of Cravens (2000) was used to estimate the volumetric emissivity of each point in the grid,

$$P = a_{cx} n_H n_{sw} \langle g \rangle, \tag{1}$$

where P is in $\mathrm{eV \cdot cm^{-3} \cdot s^{-1}}$; a_{cx}, n_H, n_{sw}, and $\langle g \rangle$, respectively, denote effective interaction factors, the density of neutral hydrogen in the exosphere, the density of solar wind ions, and the relative wind velocity. The term a_{cx} depends on the charge transfer cross section and the composition and density of highly charged ions in the solar wind. Because a_{cx} ranges from 6×10^{-16} to $6 \times 10^{-15}\mathrm{eV \cdot cm^2}$ according to Cravens (2000), we adopt $a_{cx} = 1 \times 10^{-15}\mathrm{eV \cdot cm^2}$ in this work (Jorgensen et al., 2019a). The term n_{sw} was provided by MHD simulation data, and n_H is approximated by the formula $n_H = n_0[10(R_E)/r]^3\ \mathrm{cm^{-3}}$ (Hodges, 1994; Cravens et al., 2001). The value of n_0 is 25, and $\langle g \rangle = \sqrt{u_{sw}^2 + u_{th}^2}$, which is the average collision speed estimated from the plasma bulk speed u_{sw} and the thermal speed u_{th}.

Although solar wind particles can indirectly enter the magnetosheath, the density of highly charged ions in the magnetosheath is very low, and the X-ray intensity is at least an order of magnitude smaller than outside it (Sun TR et al., 2015). As such, X-ray emissivity inside the magnetopause was ignored, and the magnetic flux method was used to locate the magnetopause in the MHD model. More specifically, from the magnetosheath to the magnetosphere, the plasma flux (density × velocity) sharply decreases at the magnetopause. The position where this flux was reduced to half the solar wind level was considered the magnetopause boundary, an approach that produced a relatively smooth magnetopause. Once this boundary was identified, X-ray emissivity inside the magnetopause was set to 0 (Jorgensen et al., 2019a). And our magnetospheric mask (the region where the emissivity is set to be zero) does not include the cusps, whereas other studies (Sun TR et al., 2019; Samsonov et al., 2022) do include the cusps. Figure 1 shows the scope of 3-D magnetospheric X-ray emissivity used in this paper and visualizes the 3-D shape of the magnetopause.

2.2 X-Ray Intensity

The SXI on the SMILE satellite collects information concerning the position of the magnetopause and bow shock during SWCX processes in the magnetosheath. Solar wind charge exchange occurs when a highly charged solar wind ion (such as O^{7+}) encounters a neutral atom (such as H) and captures an electron that stays in the excited state. This can be represented as

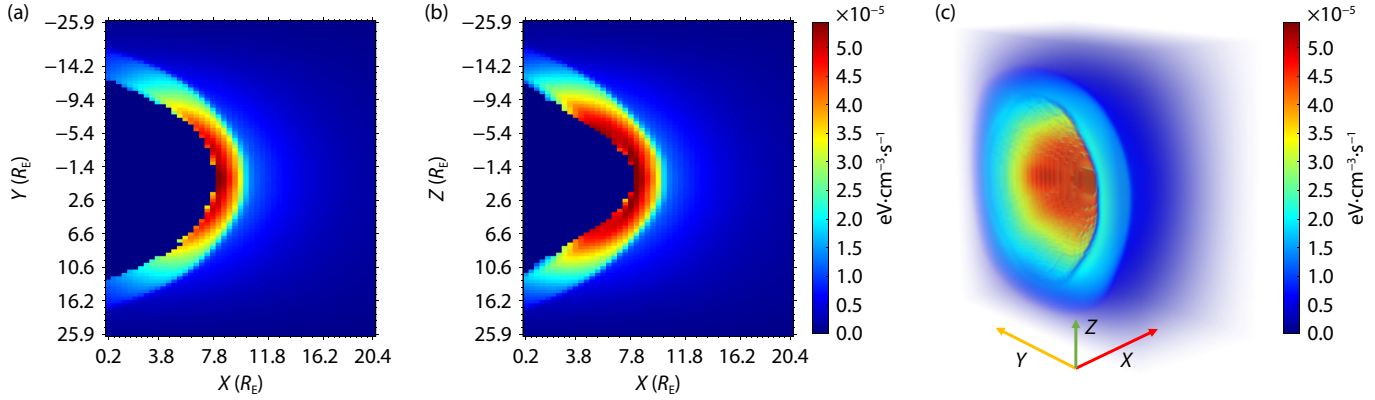

Figure 1. Three-dimensional (3-D) simulation data (X-ray emissivity) produced by the PPMLR-MHD model. Solar wind conditions: V_x = 600 km/s, N = 10 cm^{-3}, B_z = 0 nT. Size of the simulation data: 49 × 94 × 94; X-axis range: –0.2 to 20.4R_E; Y- and Z-axis range: –25.9 to 25.9R_E. (a) X–Z section of the 3-D magnetospheric X-ray emissivity data for Y = –0.2 R_E; (b) X–Y section of same region for Z = –0.2R_E; (c) 3-D view.

$$O^{7+} + H \rightarrow O^{6+*} + H^{+}. \quad (2)$$

When an ion decays to a lower energy state, it releases a photon, and the SXI detects the resulting soft X-rays. The SXI measures the integrated X-ray intensity along the look direction of a pixel. The path integrals of X-rays emitted at different distances from the charge-coupled device (CCD) in the line of sight are

$$I = \frac{1}{4\pi}\int P\mathrm{d}r = \frac{1}{4\pi}\int a_{cx} n_H n_{sw} \langle g \rangle \mathrm{d}r, \quad (3)$$

where I is in keV · cm^{-2} · s^{-1} · sr^{-1}; P is the local volume energy production rate (Figure 1), and a_{cx}, n_H, n_{sw}, and $\langle g \rangle$ have the same meaning as in Equation (1) (Cravens, 2000). We used X-ray emissions under different solar wind conditions, as shown in Table 1, to simulate 2-D X-ray images. In previous work, the ray-tracing imaging simulation method of the lobster-eye model based on the MHD model was studied and has been widely used (Peng SW et al., 2018; Sun TR et al., 2019, 2020). By specifying the position of the spacecraft and the direction of the SXI, the 2-D X-ray intensity image of the MHD model at the specified position on the SMILE operation orbit can be obtained according to Equation (3). The lobster-eye imaging principle and integrated imaging process are shown in Figure 2.

On this basis, through the instrument computer simulation of the SXI payload, combined with the relevant set of parameters, a soft X-ray photon counting image that we expect to be observed by the hypothetical SXI can be obtained. The methods and parameters used in this paper are consistent with the simulation principles and parameter settings of Guo YH et al. (2022). The observation results will be affected by the sky background, so it is necessary to add this background to the computer simulation results to achieve observation results closer to the real situation (Guo YH et al., 2021). In the soft X-ray band, the sky background is primarily a diffuse astrophysical X-ray background, and NASA's High Energy Astrophysical Science Archives Research Center (HEASARC) provides an X-ray Sky background tool (Sabol and Snowden, 2019) to calculate the average X-ray background count rate from the ROSAT (Röntgensatellit) All-Sky Survey diffuse background image. The sky background will change with the satellite orbit view, and its influence on the observation results should be reduced or possibly removed from the final imaging results of the magnetosheath. With the aforementioned tools, the intensity of the soft X-ray background within the energy range of SXI (0.2–

Table 1. Solar wind condition parameter setting of the MHD model.

Set class	Case	Number density (cm^{-3})	Velocity (km·s^{-1})	B_x (nT)	B_y (nT)	B_z (nT)
Training set	1	5	800	0	10	0
	2	5	900	0	0	5
	3	7	500	5	0	0
	4	10	400	0	0	0
	5	15	400	0	0	15
	6	15	800	0	0	10
	7	20	400	0	−10	−5
	8	20	800	0	10	−15
Test set	1	5	600	0	0	0
	2	10	600	0	0	0
	3	15	600	0	0	0
	4	20	600	0	0	0

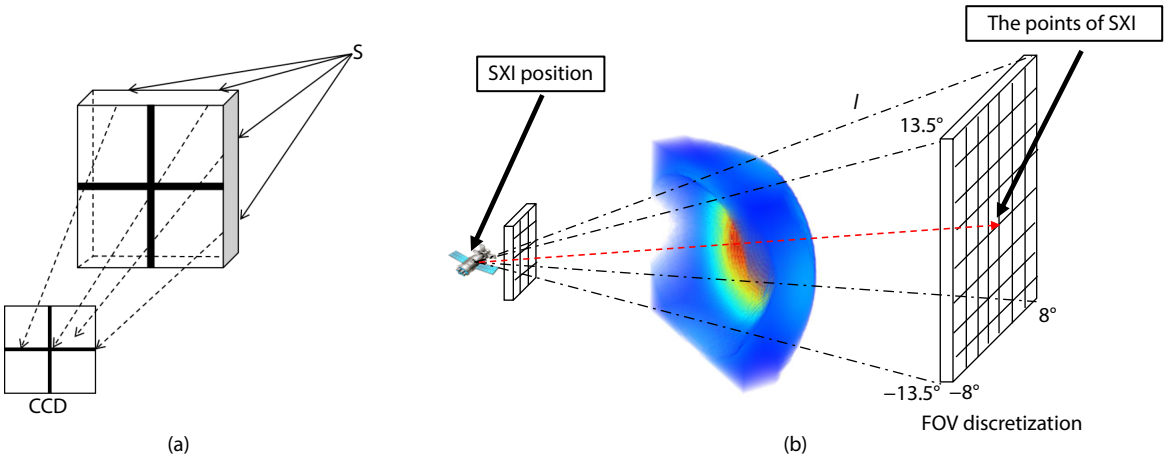

Figure 2. (a) Lobster-eye imaging principle; (b) X-ray intensity image simulation process.

5 keV soft X-ray) can be conservatively estimated to be approximately 50 keV·cm^{-2}·s^{-1}·sr^{-1}. The soft X-ray energy background has a spectral shape similar to the emission of the SWCX, but the expected maximum pixel background count is about half that of the SWCX, and the signal-to-noise ratio is approximately $40/\sqrt{40+20}$ ~ 5 sigma (Guo YH et al., 2022) at the integration time of 300 s (which is used in this work). The foreground SWCX emission is therefore easily detectable above the background.

Figure 3 shows the 2-D MHD X-ray images, with the X-ray emissivity integrated along the line of sight by using Equation (3), under different solar wind conditions and the corresponding computer simulation of SXI photon count images. Twelve sets of solar wind conditions are shown in Table 1. These 2-D MHD X-ray images and SXI photon count images obtained at different positions under solar wind conditions in Table 1 were used in the experiments described here.

We randomly selected X-ray images of 8 solar wind conditions for training, and the purpose of the test set was to train the patch estimator described in Section 3.3. One purpose of our experiment was to explore the restoration effect of the proposed restoration method on SXI photon count images under different number densities. Therefore, we selected four sets of X-ray images with different number densities and other parameters consistent with the solar wind conditions as the test set for image restoration methods. Figure 3 shows the integrated X-ray emissivity and SXI count maps for the observation point at (−3.5173, 2.6647, 19.5233) R_E in the Geocentric Solar Magnetospheric (GSM) coordinate system. The FOV of the SXI is 16° × 27° (the FOV range is −8° to 8° in the θ direction and −13.5° to 13.5° in the ϕ direction), and the center is oriented toward the target point (10.8593, 0.0157, 0) R_E. All the aforementioned values are real orbit data that may be used in SMILE satellite missions in the future.

From a visual perspective, with the increase in the solar wind number density, the effective pixel information in the 2-D MHD X-ray images retained by the SXI photon count images also gradually increases. This also means that the SXI photon count images with a high number density are less difficult to restore than those with a low number density. Because of the high number density, the available prior information on the SXI photon count images is more sufficient. However, the information around the edges of the SXI photon count images with all number densities has largely been lost because of the geometry of the lobster-eye system and the photon count distribution. Restoring this edge information in the SXI photon count image is a key task in this work.

2.3 Image Analysis

The distribution of pixel values is a basic method used to describe an image. By comparing the distribution of pixels between images, we can measure their degree of similarity and judge whether a simple mapping relationship exists. Figure 4 shows the histograms of photon numbers (and the integrated emissivity distribution) for the three scenarios presented in Table 2.

Scenario 1: Comparing MHD X-ray images from the same solar wind conditions and location, the SXI photon count image without a sky background, and the SXI photon count image after adding a constant sky background pixel value distribution.
Scenario 2: Analyzing the distribution of pixel values of SXI photon count images after adding a constant sky background under the same solar wind conditions. The position coordinates and aim points of the SXI in the GSM coordinate system are shown in the table.
Scenario 3: Comparing the SXI photon count images after adding a constant sky background with different solar wind number densities at the same location.

Figure 4a illustrates the corresponding results for Scenario 1. Our purpose was to explore whether a simple linear mapping relationship (similar pixel distribution) would exist between the MHD X-ray images and SXI photon count images. However, the results showed that the pixel distributions of the three histograms in Figure 4a presented different shapes. This result means that a complex underlying mapping relationship exists between them, rather than a simple linear expression relationship. The aforementioned results show that we cannot use simple mathematical models, such as Gaussian distribution fitting, to represent the mapping relationship between MHD X-ray images and SXI photon count images. This also prompted the use of the deep neural network technology presented in Section 3.3 to establish a potentially complex mapping relationship between the two image patches.

Figures 4(b1)–(b3) show the pixel distributions corresponding to

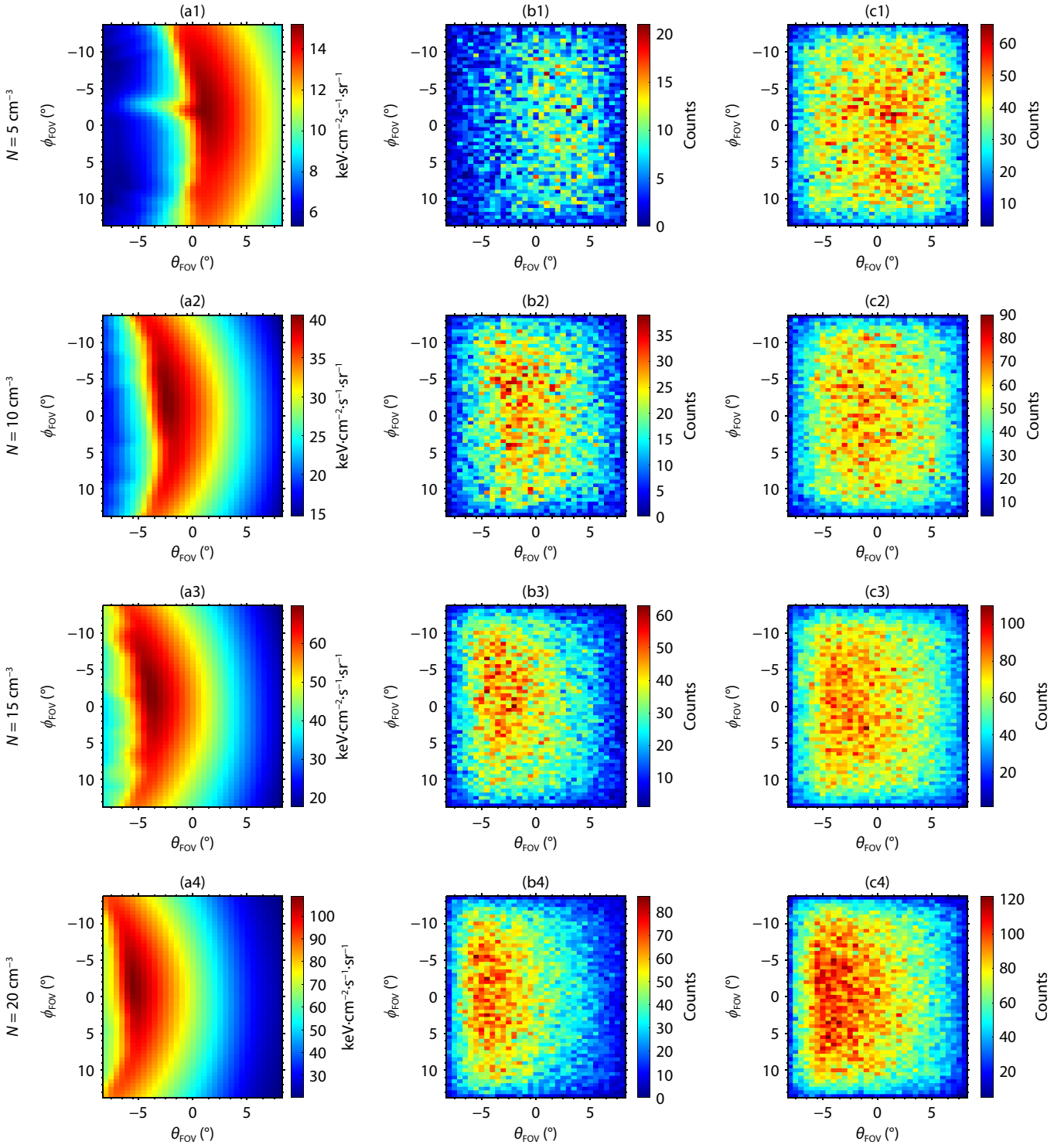

Figure 3. (a1)–(a4) The MHD X-ray image inside the FOV with the solar wind number density 5, 10, 15, and 20 cm^{-3}; (b1)–(b4) the SXI photon count image corresponding to (a1)–(a4) without the sky background; (c1)–(c4) the SXI photon count image corresponding to (a1)–(a4) after adding the constant sky background, which was obtained by inputting (a1)–(a4) with the constant sky background into the SXI imaging simulation technology (Guo YH et al., 2022). The SXI simulation integration time is 300 s, and other solar wind conditions are V_x = 600 km/s and B_z = 0 nT. The size of the images is 55 × 33. The range of the FOV angle is −13.5° to 13.5° and −8° to 8°, so the resolution is 0.5°. The intensity of the sky background on panels (c1)–(c4) is approximately $40/\sqrt{40+20} \sim 5$ sigma.

Scenario 2. Their distributions are remarkably similar, which indicates that the degradation matrix $\boldsymbol{H}$ in the degradation model ($\boldsymbol{y} = \boldsymbol{Hx} + \boldsymbol{e}$) with the same instrument parameters of SXI does not change with the observation position. This also means that it is not necessary to retrain the deep neural network model because of the change in the observation position, which is crucial for

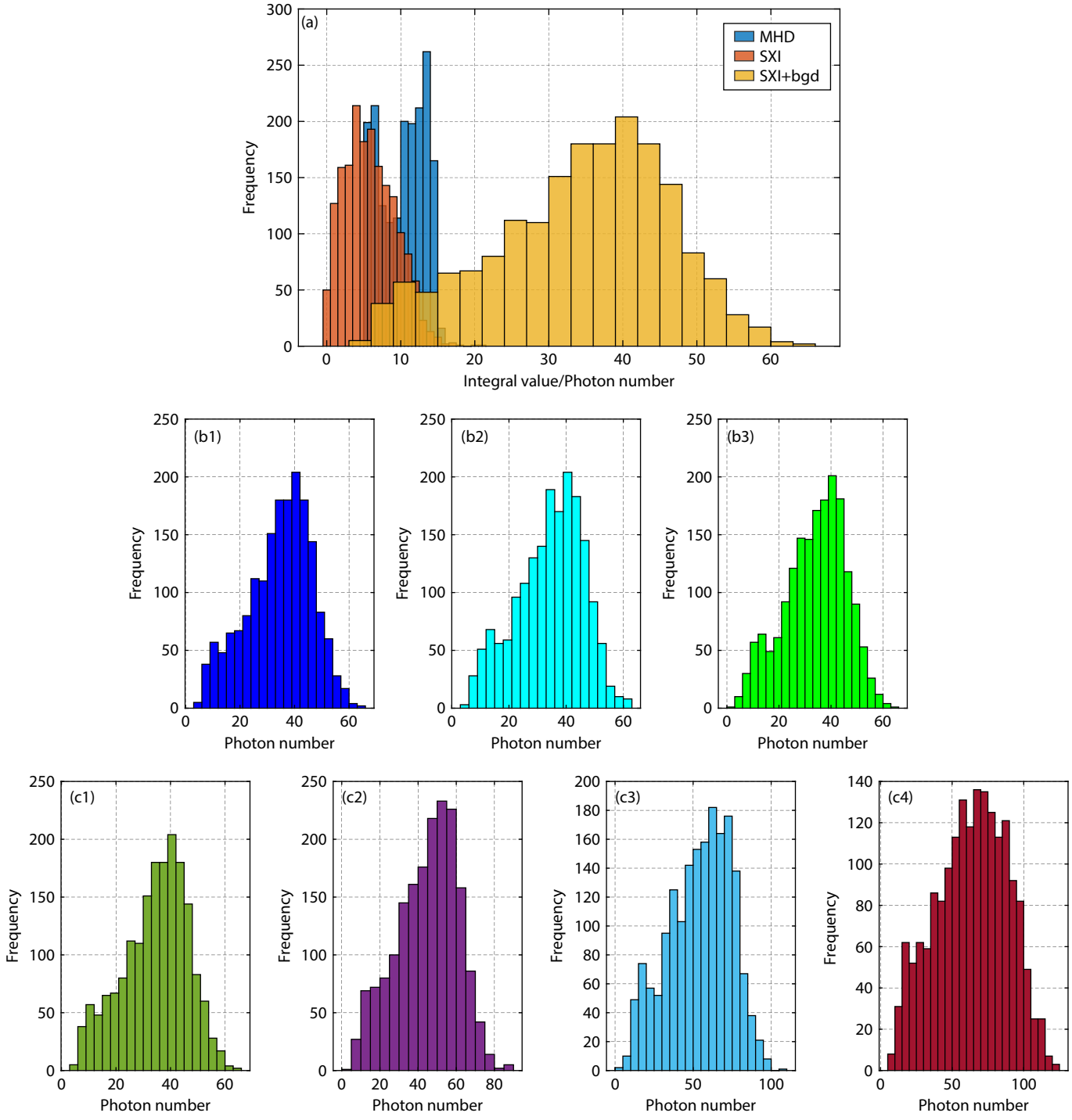

Figure 4. (a) Histogram of the pixel distribution of Scenario 1; (b1)–(b3) histogram of the pixel distribution of Scenario 2; (c1)–(c4) histogram of the pixel distribution of Scenario 3, with the corresponding solar wind number density, from left to right, of 5, 10, 15, and 20 cm^{-3}. The solar wind number density of (a) and (b1)–(b3) is 5 cm^{-3}, and other solar wind conditions for all images are V_x = 600 km/s; B_x, B_y, and B_z are equal to 0 nT.

increasing the recovery speed. Figures 4(c1)–(c4) present the pixel distributions corresponding to Scenario 3. The pixel distribution of the four images has an obvious linear mapping relationship, which also proves that the degradation matrix is unchanged from the side. With the gradual increase in solar wind number density (from left to right), the distribution of pixels remains unchanged, but the number of SXI counts (or photons) per pixel increases. This is because the SWCX process is enhanced as the solar wind number density increases, so the number of photons that can be received by the SXI detection panel gradually increases.

3. Methodology

Here, we introduce each step of the proposed photon count image restoration method and discuss its implementation.

3.1 Creating a Clean–Noise Patch Pair Dataset

A patch is a small piece of an image. To divide a patch is to divide

Table 2. Solar wind conditions, SXI position, and aim points corresponding to the three different scenarios.

Scenario	Number density (cm^{-3})	Velocity ($km·s^{-1}$)	SXI position (R_E)	SXI aim point (R_E)	Add sky background
1	5	600	(–3.5173, 2.6647, 19.5233)	(10.8593, 0.0157, 0)	Figure 4a MHD (no)
					Figure 4a SXI (no)
					Figure 4a SXI + bgd (yes)
2	5	600	(–3.5173, 2.6647, 19.5233)	(10.8593, 0.0157, 0)	Figure 4(b1) (yes)
			(–3.6941, 5.1986, 18.9843)	(10.9377, 0.0148, 0)	Figure 4(b2) (yes)
			(–3.7799, 7.5792, 17.9918)	(10.9047, 0.0122, 0)	Figure 4(b3) (yes)
3	5	600	(–3.5173, 2.6647, 19.5233)	(10.8593, 0.0157, 0)	Figure 4(c1) (yes)
	10				Figure 4(c2) (yes)
	15				Figure 4(c3) (yes)
	20				Figure 4(c4) (yes)

the original complete image into small images that are still part of the original image while the pixel value remains unchanged. Many methods can be used to divide patches, such as the random block, mirror block, and sequential block methods. We used the overlapping block method (Ronneberger et al., 2015), which divides the complete image into patches with overlapping parts. This method reduces the computation of the patch estimator and highlights the edge details of the image. Figure 5 shows the overlapping block process and parameters. In this work, the patch pairs were obtained by overlapping block technology based on the MHD X-ray images and SXI photon count images after adding a constant sky background corresponding to all the solar wind conditions shown in Table 1. A clean–noise patch pair dataset was thus established for training and experimental verification.

The initial size of the MHD X-ray images obtained in Section 2.2 is 271 × 161, whereas the size of the SXI photon count image after adding the constant sky background is 55 × 33 (Guo YH et al., 2022). This difference is due to the structure of the SXI probe. Therefore, before obtaining a patch pair, it is necessary to downsample (five-pixel sampling interval) the MHD X-ray images to reduce their size from 271 × 161 to the same size as the photon count image. Next, we defined the parameters of the overlapping block. The patches are 8 × 8, and the moving steps in the θ_{FOV} and ϕ_{FOV} directions are 5. However, it cannot be completely divided in the ϕ_{FOV} direction, and the image remains after moving to the 10th block (46–53). So as not to miss all the information in the image, we added an 11th block (48–55) in the ϕ_{FOV} direction. Thus, 66 patch pairs could be obtained for one MHD X-ray image and one SXI photon count image after adding the constant sky background.

3.2 Patch Clustering

We have many patch pairs from the MHD X-ray images and SXI photon count images after adding the constant sky background.

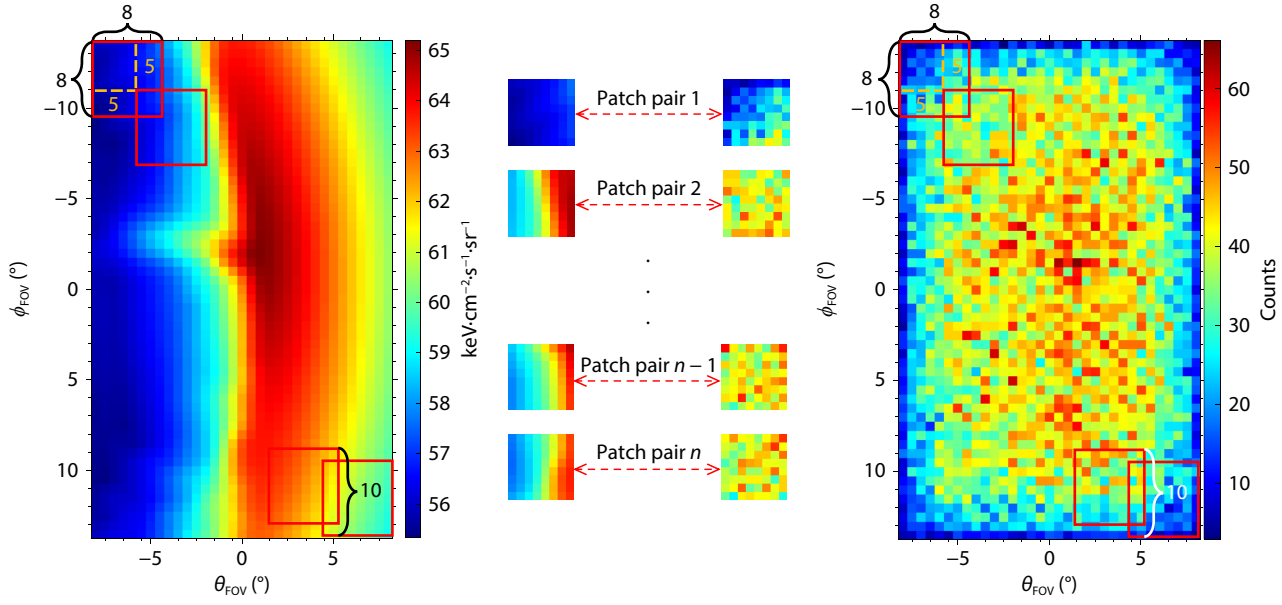

Figure 5. Obtaining a patch pair by the overlapping block technology. The size of the red squares is 8 × 8, and the movement step size is 5. The red squares in the figure are shown for purposes of illustration and do not match those used in the simulations.

Our purpose is to estimate the clean patch from the noise patch, which is the work of the patch estimator described in Section 3.3. To further reduce the working difficulty of the patch estimator and the training convergence speed, we cluster the patch pairs based on the noise patch before training the patch estimator. Patch pairs from different clusters are used to train the patch estimators. In the subsequent restoration process, the corresponding patch estimator is selected to estimate the clean patch based on the cluster of noise patches, which improves the accuracy of the patch estimator (Salimans et al., 2016).

For the clustering of patch pairs, any clustering (hard clustering) algorithm can be used, such as *k*-means, because the proposed recovery algorithm does not rely critically on clustering. We use the CEM algorithm (Celeux and Govaert, 1992), which fits K multivariate Gaussian distributions into the data and considers the samples assigned to each distribution as a cluster. Thus, the patch pairs used to train the same patch estimator follow the same multivariate Gaussian distribution.

The expectation–maximization (EM) algorithm (Dempster et al., 1977) iteratively calculates the maximum likelihood or maximum a posteriori estimates and has been widely used for image classification (Bruzzone and Prieto, 2001; Kersten et al., 2005). For the Gaussian mixture model, the EM first expresses the global distribution of a complex mixture with finite parameter distribution combinations and iteratively maximizes the expected value to gradually approximate the parameter set of the maximum likelihood function of each density distribution (Tadjudin and Landgrebe, 1996). We presume that the p-dimensional vector data $\boldsymbol{x}$ ($\boldsymbol{x} \in R^p$) are a mixture of K-component Gaussian distributions (K is set to 10 in this work). The density function is then defined as

$$f(x;\theta) = \sum_{k=1}^{K} \alpha_k f_k(x|\theta_k), \tag{4}$$

where $\alpha_1, \cdots, \alpha_K$ are the prior probabilities of each component in the mixed Gaussian model, and $\boldsymbol{\theta} = (\theta_1, \cdots, \theta_K)$ are the unknown parameters for Gaussian density functions $f_k(x|\theta_k)$, $k = 1, \cdots, K$, where K is the number of classes. The entire set of parameters for the Gaussian mixture model is $\boldsymbol{\theta} = (\alpha_1, \cdots, \alpha_K, \theta_1, \cdots, \theta_K)$, which can be rewritten as $\boldsymbol{\theta} = (\alpha_1, \cdots, \alpha_K, \mu_1, \cdots, \mu_K, \sum_1, \cdots \sum_K)$, and $\mu_1, \cdots, \mu_K$ and $\sum_1, \cdots \sum_K$ are the mean and covariance matrices, respectively, of each cluster sample. Hence, samples can be classified by estimating the parameters of the Gaussian mixture model. For unclassified datasets $\{x_1, \cdots, x_n\}$ (534,864 noise patches), the maximum likelihood estimation of $\boldsymbol{\theta}$ can be determined as

$$\theta_{ML} = \arg\max_{\theta} \prod_{i=1}^{n} f(x_i|\theta), \tag{5}$$

which is an incomplete data problem lacking observational information (McLachlan and Peel, 2000), for which it is difficult to solve directly for x_i; $f(\boldsymbol{x}|\boldsymbol{\theta})$ is the conditional probability of $\boldsymbol{x}$ if $\boldsymbol{\theta}$ has a definite distribution. The EM is a general algorithm to compute maximum likelihood estimates of α_k, $\theta_k (1 \leqslant k \leqslant K)$ under the mixture approach. The CEM is also a general algorithm for estimating α_k, θ_k and finding clusters $P_k (1 \leqslant k \leqslant K)$ under the classification approach. The EM algorithm has an expectation step (E-step) and a maximization step (M-step), whereas the CEM incorporates a classification step (C-step) between the E-step and M-step by using the maximum a posteriori principle. We define the number of clusters K and initialize the parameters α_k, μ_k, $\sum_k (1 \leqslant k \leqslant K)$ for each cluster. Starting from an initial partition P^0, the lth iteration of the CEM ($l > 0$) is defined as follows:

E-Step. Compute for $i = 1, \cdots n$ and $k = 1, \cdots K$ the current (l iteration) posterior probability $\gamma_k^l(x_i)$ that x_i belongs to P_k,

$$\gamma_k^l(x_i) = \frac{\alpha_k^l f\left(x_i \middle| \mu_k^l, \sum_k^l\right)}{\sum_{k=1}^{K} \alpha_k^l f\left(x_i \middle| \mu_k^l, \sum_k^l\right)}. \tag{6}$$

C-Step. Assign each x_i to the cluster that provides the maximum posterior probability $\gamma_k^l(x_i)$, $1 \leqslant k \leqslant K$. (If the maximum posterior probability is not unique, choose the cluster with the smallest index.) Let P_k^l denote the resulting partition.

M-Step. For $k = 1, \cdots K$, compute the maximum likelihood estimates (α_k^{l+1}, μ_k^{l+1}, and $\sum_k^{l+1}$) by using subsamples P_k^l,

$$N_k = \sum_{x_i \in P_k^l} \gamma_k^l(x_i), \tag{7}$$

$$\alpha_k^{l+1} = \frac{N_k}{N_{x_i \in P_k^l}}, \tag{8}$$

$$\mu_k^l = \frac{1}{N_k} \sum_{x_i \in P_k^l} \left[\gamma_k^l(x_i) \cdot x_i\right], \tag{9}$$

$$\sum_k^{l+1} = \frac{1}{N_k} \sum_{x_i \in P_k^l} \left[\gamma_k^l(x_i) \cdot \left(x_i - \mu_k^l\right)\right], \tag{10}$$

where $N_{x_i \in P_k^l}$ is the number of $x_i \in P_k^l$. Updated estimates of unknown parameters are obtained according to Equations (7)–(10) and used to calculate the corresponding log-likelihood,

$$L = \prod_{i=1}^{n} \sum_{k=1}^{K} \left[\alpha_k^l \cdot f\left(x_i \middle| \mu_k^l, \sum_k^l\right)\right]. \tag{11}$$

With each iteration, the set of estimated parameters provides an increased log-likelihood until a local maximum is reached. Convergence is reached when the relative increase in the log-likelihood is less than a specified threshold ε, namely,

$$\left\|L^{k+1} - L^k\right\| \leqslant \varepsilon, \tag{12}$$

where ε (set as 10^{-4}) is an arbitrarily small positive threshold. If the relative increase of the log-likelihood function is greater than ε, then the E-step, C-step, and M-step are repeated until the specified condition is reached. In this section, we introduce the mathematical principles and derivation of the CEM algorithm. The CEM algorithm is used in this work to classify large-scale noise image patches, and the classified noise image patches are used to train the estimator described in Section 3.3.

3.3 Patch Estimator

Pixel estimation is crucial in traditional filtering restoration methods because it estimates the center pixel by using the weighted average of adjacent pixels (Lebrun, 2012; Yan RM et al., 2014). The I-NLM and block matching 3-D (BM3D) algorithms (Dabov et al., 2007) replace central pixel estimation with patch estimation in the

image. However, they rely on prior knowledge of the degraded image itself, which limits recovery performance. With the idea of E-NLM, restoration algorithms began to rely on prior knowledge of the external datasets for the restoration estimation of degraded image patches (Levin and Nadler, 2011). A variety of image restoration algorithms based on E-NLM have achieved remarkable results in various image restoration tasks.

Generative adversarial networks have brought rapid development to various fields of degraded image restoration. They find the mapping relationship between a degraded image and the original image by training a deep neural network. The original GANs used random noise images to generate images similar to a real image distribution (Goodfellow et al., 2014; Radford et al., 2016). However, the input of the image restoration task was not random noise but the observed degraded image, so it was necessary to provide the degraded image and the corresponding original image to the network to enable it to learn the one-to-one correspondence between them. The emergence of conditional GANs solves the aforementioned problems (Mirza and Osindero, 2014). Isola et al. (2017) developed the pix2pix project, which uses the conditional generation countermeasure network technology to realize the generation task from one type of image to another. This project has brought new inspiration to image restoration.

We constructed a patch estimator to estimate patches from degraded image patches based on the pix2pix project. The patch estimator includes a generator G and discriminator D. The generator restores clean patches corresponding to noise patches and includes encoding and decoding procedures. Encoding is based on downsampling and provides feature mapping to the symmetric layer of the decoding process, which adopts upsampling and nonlinear spatial transmission. We use the encoder–decoder model for the generator, which has a U-Net structure of 8- and 7-layer decoders with a deconvolution layer. The discriminator distinguishes between true and false images and applies a sigmoid function to the last layer in feature mapping so that the probability score can be changed to [0, 1] because the results of the clean and generated patches are similar in texture and each pixel is closely related to its surrounding pixels. We use the Markov discriminator PatchGAN (Pathak et al., 2016), which models the image into a Markov random field; a pixel with a distance greater than one patch is independent, and those with a distance within one patch are related. The PatchGAN discriminator does not impose a size restriction on the patch and maintains the high resolution and texture structure of the patch, and it can effectively reduce the number of parameters and calculations. Figure 6 shows the structure of the patch estimator.

The training data for the patch estimator have paired patches (x, y; noise–clean patch pairs), where x (noise patch) is the input of the generator G, and y (clean patch) is the target image patch. When training the generator, we randomly input a mix of x and z (random noise patch) so that it can obtain a more diverse output and improve its generalization ability. Without adding z, the patch estimator can still learn the mapping from x to y, but this will produce a deterministic output, resulting in the inability to match any distribution other than the pulse function. The output of the generator is $G(x)$, which is combined with x as the input to the discriminator to obtain the prediction probability $D(G(x), x)$, which is the probability that the input is a pair of real images. The closer the probability is to 1, the more certain the discriminator is that the input is a real pair of images. In addition, y and x are combined as positive samples to serve as the input of the discriminator D. The positive samples give the discriminator a judgment criterion and guide it to make a judgment. Hence, the training goal of the discriminator is to output a small probability value (close to 0) when the input is not a pair of real images (x and $G(x)$) and a large probability value (close to 1) when the input is a pair of real images (x and y). The training goal of the generator is to generate $G(x)$ and x as inputs to the discriminator and maximize its output probability, that is, to deceive the discriminator. The purpose of the discriminator is to distinguish between x and $G(x)$, which give lower probability values, and x and y, which give higher probability values. The generator and discriminator are trained iteratively with each other in the game. When an equilibrium point is reached, then the network has reached convergence and the iterative training can be stopped. This is the Nash equilibrium (Nash

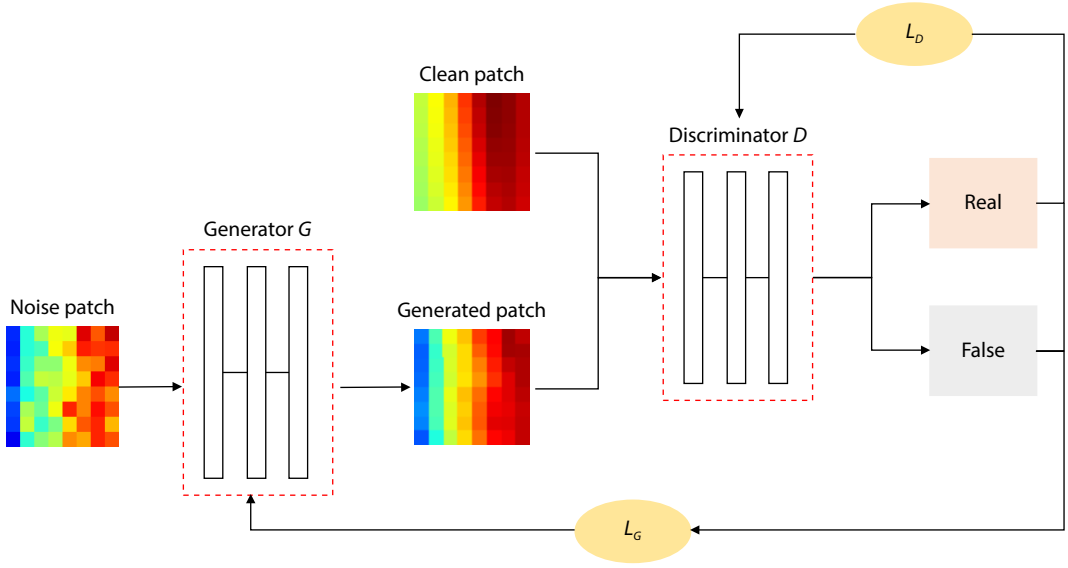

Figure 6. Structure of the patch estimator.

et al., 1950). Figure 7 shows the entire process of patch input and output to the estimator network. At the same time, the detailed structure of the estimator network (PyTorch framework) is given, which provides ideas and a basis for reproducing the estimator network.

The purpose of the patch estimator is to learn the mapping from a noise patch to a clean patch and train the generator and discriminator by using the loss function L_G, which consists of adversarial loss L_{adv} and pixel loss L_{pix},

$$L_{adv} = -E_{x\sim P_{data}(x),z\sim P_{data}(z)}\left[\log D\left(x, G\left(x, z\right)\right)\right], \tag{13}$$

$$L_{pix} = -E_{x\sim P_{data}(x),y\sim P_{data}(y),z\sim P_{data}(z)}\left[\left\|y - G\left(x, z\right)\right\|_1\right], \tag{14}$$

$$L_G = L_{adv} + \lambda \cdot L_{pix}, \tag{15}$$

where E is the expectation; $x\sim P_{data}(x)$ is the distribution of the noise patch dataset; $y\sim P_{data}(y)$ is the distribution of the clean patch dataset; $z\sim P_{data}(z)$ is the distribution of random noise, which is Gaussian; and λ is a regularization parameter used to balance the loss function, which we set to 10. The purpose of adversarial loss L_{adv} is to deceive the discriminator as much as possible by the output $G(x)$ of the generator, whereas pixel loss L_{pix} constrains the L1 distance between the generated image $G(x)$ and y (clean patch) to make them as similar as possible. The loss function L_G of the generator is the objective function of its training. The loss function of the discriminator is defined by the confrontation between the generator and discriminator,

$$\begin{aligned} L_D = {} & E_{x\sim P_{data}(x),y\sim P_{data}(y)}\left[\log D\left(x, y\right)\right] + \\ & E_{x\sim P_{data}(x),z\sim P_{data}(z)}\left[\log\left(1 - D\left(x, G\left(x, z\right)\right)\right)\right], \end{aligned} \tag{16}$$

where x and y are input to the discriminator as positive samples, and X, $G(x)$, z, and $G(z)$ are input as negative samples. Positive samples provide criteria for the discriminator, and negative samples provide much discriminant experience for discriminator training. Thus, the final objective function of the patch estimator is

$$\hat{G} = \arg\min_G \max_D \left(L_G + L_D\right). \tag{17}$$

The purpose of the objective function is to minimize L_G and maximize L_D. In this way, the generator can obtain an estimated patch similar to clean patches by inputting noise patches. The estimated patch can obtain a higher output value under the identification of the discriminator. Thus, the patch estimator can learn the potential mapping relationship between noise patches and clean patches and achieve the purpose of estimating clean patches by noise patches.

3.4 Practical Implementation Process

We discussed the acquisition of noise–clean patch pairs in Section 3.1. These pairs must be obtained from the corresponding MHD X-ray images and SXI photon count images after adding the constant sky background. X-ray emissions under all solar wind conditions corresponding to Table 1 are used to obtain MHD X-ray images and SXI photon count images after adding the constant sky background, as described in Section 2.2. In Section 4.3, we discuss coordinate information on the observation points. Thus, we can obtain large-scale noise–clean patch pair datasets for subsequent clustering, patch estimator training, and experimental testing.

The number of clusters and the initial mixed distribution parameters corresponding to each cluster in the CEM algorithm should be set in advance. The number of clusters K is 10, and the initial distri-

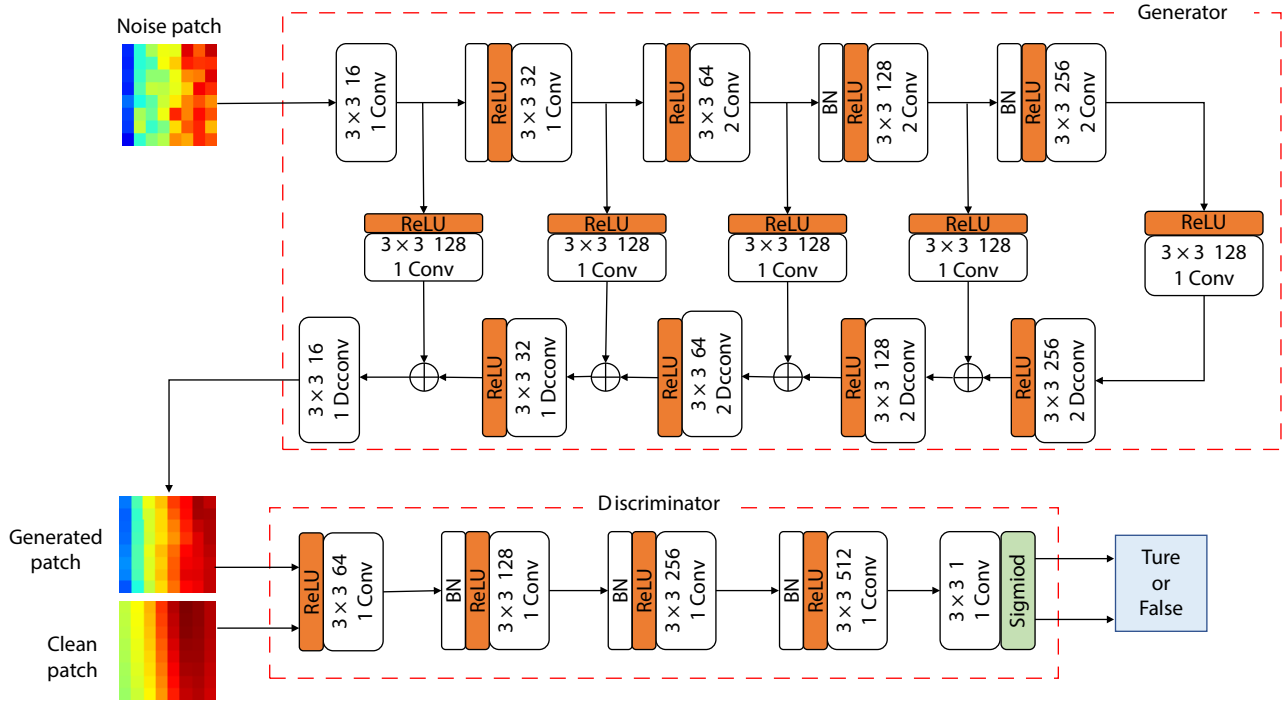

Figure 7. Training a patch estimator to map the noise patch to a clean patch. ReLU (Rectified Linear Unit) is a nonlinear activation function in neural networks. And BN (Batch normalization) is a data processing method for optimizing neural networks.

bution parameters of each cluster are estimated by randomly extracting 10 noise patches from the dataset of noise patches awaiting classification. The fixed threshold ε is set to 10^{-4}. We set the maximum number of iterations to 1000 to prevent an infinite cycle caused by the failure to converge.

Noise–clean patch pairs were divided into 10 clusters by the CEM algorithm; hence, we needed to train 10 patch estimators. We used 10 noise–clean patch pair clusters obtained by CEM to train 10 patch estimators, and the relevant parameters used in the training process of the 10-patch estimator remained consistent. The training epochs were set to 2000, and the batch size was 16. The initial learning rate of a gradient descent-based optimization method (Adam) was set to 0.0002, and the Adam movement was set to 0.5 (Kingma and Ba, 2017). The learning rate remained unchanged in the first 1000 epochs and decreased linearly to 0 in the last 1000 epochs. The loss coefficient of L1 of the generator was set to 10. We used the PyTorch deep learning framework (Paszke et al., 2019) to build the patch estimator on a 64-bit Windows 10 operating system. A GPU was used in the training process, the graphics card model was RTX 3090, the video memory size was 24 GB, and the virtual environment was Anaconda, PyTorch 1.8.1, and CUDA 11.0.

In the final estimation of the noise patches of the test set, an SXI count map was partitioned after adding the constant sky background according to the overlapping block technology described in Section 3.1. The patch estimator of the corresponding cluster was then matched according to the CEM algorithm, and the noise patches were estimated, one by one, to obtain the restored patches, which composed a completely restored image following the original position. Because we used overlapping blocks, the patches had overlapping areas. The recovery value of overlapping areas was estimated by utilizing the average value. We used an adaptive smoothing filter (Ferrara, 1980) to smooth the restored image and obtain the final restored result.

4. Experimental Results

In this section, we evaluate the performance of the proposed image restoration method on the SXI count map dataset. We also show the reconstruction effect of the reconstructed images applied to two common magnetopause X-ray emissivity reconstruction techniques, the tangent fitting approach (TFA) and the CTA.

4.1 Preparation of the Experimental Data

The 12 solar wind conditions in Table 1 are divided into two parts, 8 as a training set and 4 as a test set. Twelve X-ray emission values corresponding to solar wind conditions were used to make MHD X-ray images and SXI photon count images after adding a constant sky background at different observation positions. Different observation positions on the two orbits are used in this work, as shown in Figure 8.

The black dotted line indicates the simulated orbit that SMILE is expected to use after launch, and it approximates a large ellipse. The points of the SXI on SMILE are constantly changing based on the simulation of actual satellite missions. The SMILE satellite plans to operate in the orbit shown in Figure 8a, with a sampling interval of 3 min and a total of 1041 sampling points. Because the imaging results of the SXI reflect a more complex situation when the satellite is close to the interior of the Earth's magnetopause, these results not meaningful for the reconstruction of the 3-D Earth magnetopause profile. Therefore, only 757 sampling points larger than 10 R_E along the Z-axis in the GSM coordinate system are reserved, corresponding to the green points in Figure 8a. The orbit in 8a corresponds to one orbital period in the candidate orbit. The other orbit (Figure 8b) is semicircular, with a radius of 80 R_E, with (9.8, 0, 0) R_E as the center of the circle and the fixed points of SXI. Its polar coordinate equation is

$$\begin{cases} x = 9.8 \\ y = r_2 \cdot \cos(\beta) \\ z = r_2 \cdot \sin(\beta) \\ r_2 = 80,\ \beta \in \left(\dfrac{\pi}{2}, \dfrac{3\pi}{2}\right) \end{cases}. \tag{18}$$

The semicircular orbit corresponds to the red dotted line in

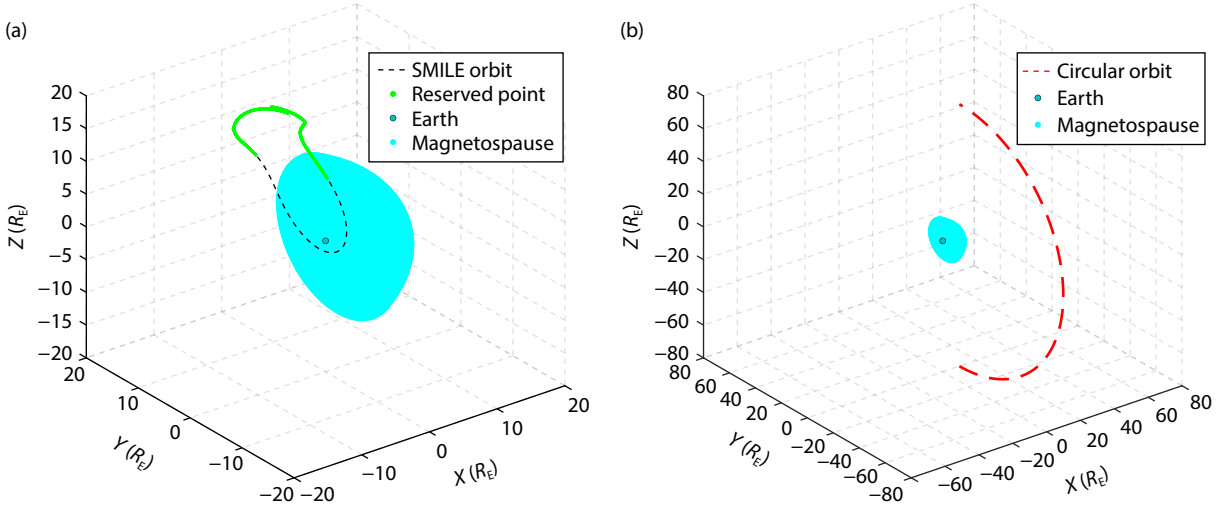

Figure 8. (a) Expected partial SMILE orbit; (b) a circular orbit used in the CTA reconstruction. The coordinate system is GSM. The cyan scatter is calculated using the magnetopause model of Shue et al. (1997).

Figure 8b. The sampling interval is 0.7059°, and there are 256 sampling points. The images obtained from the observed position reserved for the SMILE orbit (green dot) are used in the SXI photon count image restoration experiment and TFA analysis experiment described in Sections 4.2 and 4.3. The images of the observed position corresponding to the semicircular orbit (red dotted line in Figure 8b) are used to support the CTA reconstruction experiment presented in Section 4.4.

We used the simulated X-ray emissions to obtain 2-D MHD X-ray images corresponding to 1013 observation positions, whereas we used the SXI analog imaging technique mentioned in Section 2.2 to obtain the corresponding soft X-ray photon count map (with added sky background). These images can be used to make 534,864 noiseless patch pairs. The pairs are divided into 10 clusters by the CEM algorithm to train 10 patch estimators. Ten patch estimators participated in the estimation of 4052 SXI photon count images after adding the constant sky background in the test set.

4.2 SXI Photon Count Image Restoration

Here, we apply the proposed method to the restoration task of the test set image. In addition to our proposed method, the restoration results of some classical image restoration methods are presented, including BM3D (Dabov et al., 2007), weighted nuclear norm minimization (WNNM; Gu SH et al., 2014), I-NLM (Buades et al., 2005), and K-singular value decomposition (K-SVD; Aharon et al., 2006). Figure 9 shows the restoration results of the

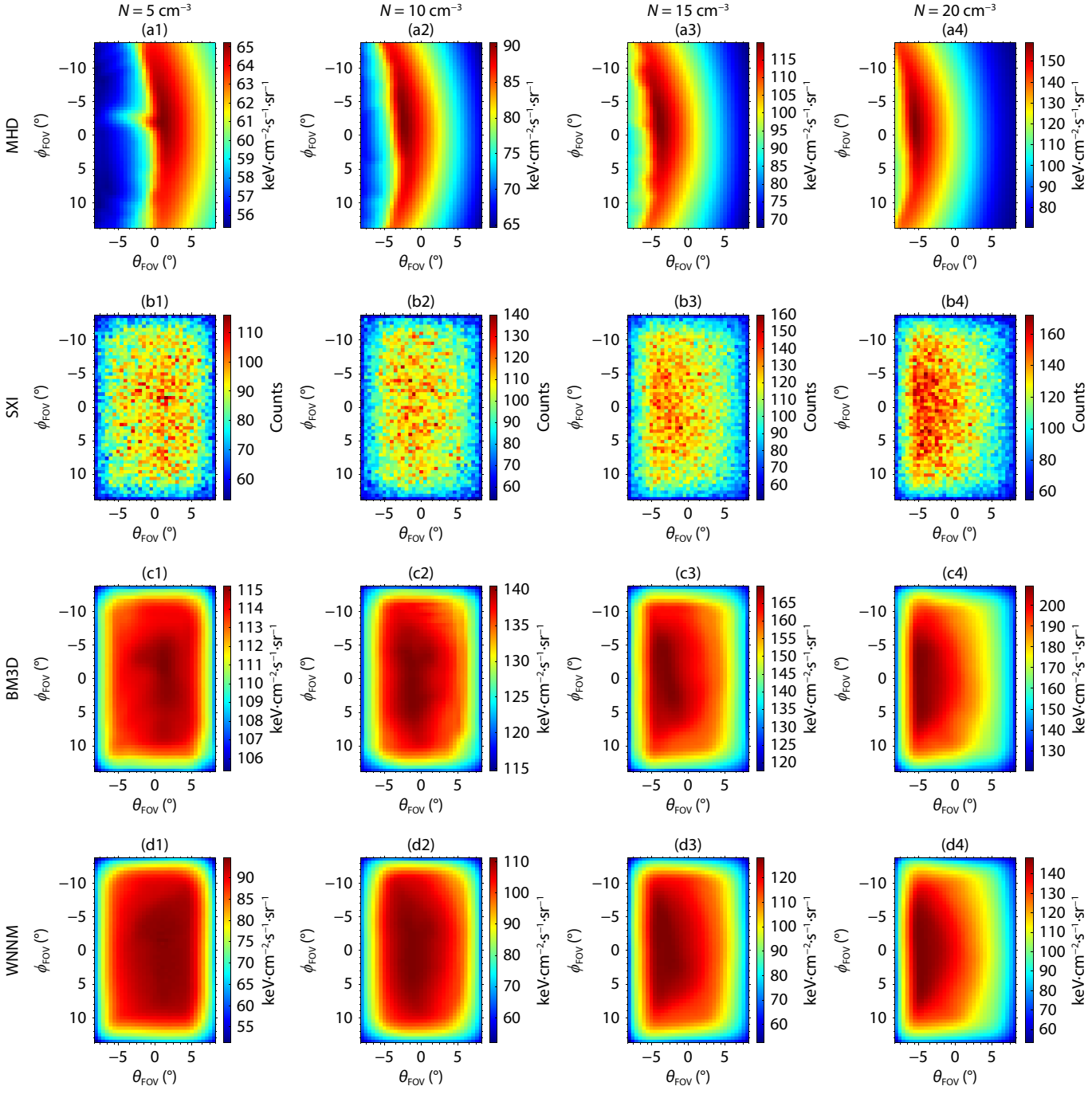

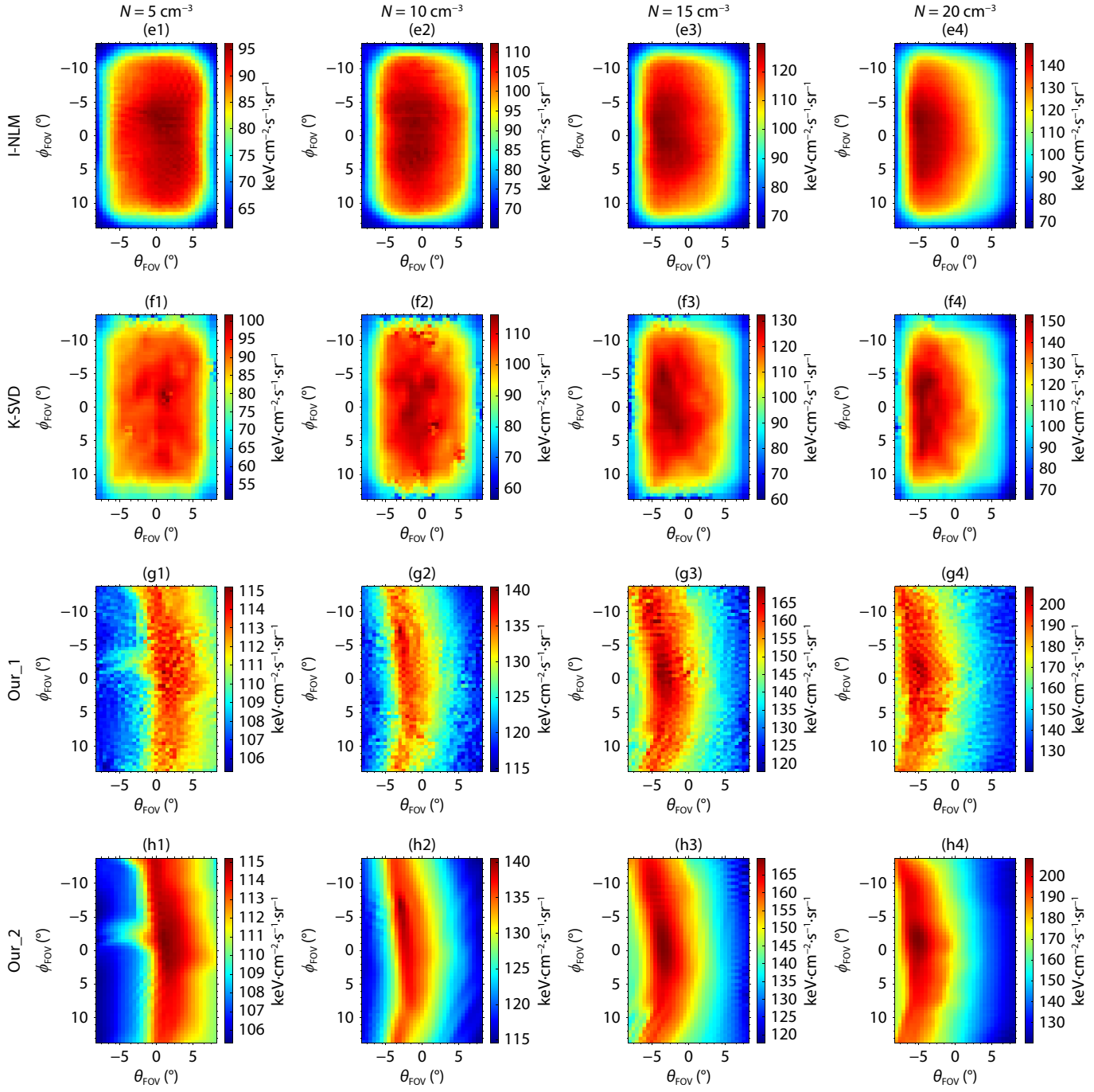

Figure 9. (a1)–(a4) MHD X-ray images after adding the constant sky background; (b1)–(b4) SXI photon count images after adding the constant sky background; (c1)–(c4) restoration result obtained by BM3D; (d1)–(d4) restoration result obtained by WNNM; (e1)–(e4) restoration result obtained by I-NLM; (f1)–(f4) restoration result obtained by K-SVD; (g1)–(g4) restoration result before smoothing, as obtained by the proposed restoration algorithm; (h1)–(h4) restoration result after smoothing, as obtained by the proposed restoration algorithm. Columns from left to right correspond to solar wind number densities N = 5cm^{-3}, N = 10cm^{-3}, N = 15cm^{-3}, and N = 20cm^{-3}, respectively. Other solar wind conditions are V_x = 600 km/s and B_z = 0 nT.

SXI photon count images after adding the constant sky background, with the observation position of (–3.5173, 2.6647, 19.5233) R_E and the SXI aim point of (10.8593, 0.0157, 0) R_E.

The evaluation indexes used in this paper include the peak signal-to-noise ratio (PSNR) and structural similarity (SSIM). The PSNR is a common objective image evaluation index used to measure the quality of restored images,

$$Q_{\mathrm{PSNR}}(X,R) = 10\cdot\log_{10}\frac{PL^2}{||X-R||}, \tag{19}$$

where X is the image to be compared, R is the reference image, L is the maximum value of the reference image, and P is the number of pixels. In general, a PSNR value higher than 40 dB is considered

an excellent restoration effect, 30 to 40 dB represents a good restoration effect, 20 to 30 dB represents a qualified restoration effect, and a restoration effect below 20 dB is considered unqualified. The SSIM measures the structural similarity of two images, usually of the same size, or is used to detect the degree of image distortion:

$$Q_{\mathrm{SSIM}}(f_1, f_2) = \frac{(2\mu_{f_1}\mu_{f_2} + C_1)(2\sigma_{f_1 f_2} + C_2)}{(\mu_{f_1}^2 + \mu_{f_2}^2 + C_1)(\sigma_{f_1}^2 + \sigma_{f_2}^2 + C_2)}, \tag{20}$$

where μ_{f_1} and $\sigma_{f_1}^2$ are the mean and variance, respectively, of f_1; μ_{f_2} and $\sigma_{f_2}^2$ are the mean and variance, respectively, of f_2; f_1 is the image to be compared and f_2 is the reference image; $\sigma_{f_1 f_2}$ is the covariance between f_1 and f_2; and $C_1 = (K_1 L)^2$ and $C_2 = (K_2 L)^2$ are constants used to maintain stability. Generally, $K_1 = 0.01$, $K_2 = 0.03$ (as in this work), and L is the maximum value in the data. The SSIM generally ranges between 0 and 1, and the closer to 1, the greater the similarity. However, if two structures are completely unrelated (negative correlation), the SSIM can be less than 0.

When calculating the PSNR and SSIM, considering that the pixel value ranges of different restoration results are inconsistent, we uniformly map MHD X-ray images and each restoration result to the range of 0–255, and then calculate the PSNR and SSIM. Hence, L is 255. Figure 10 shows the distribution of evaluation indicators of the restoration results for the various restoration methods. One box plot represents the distribution of evaluation indicators for 757 restored images.

Two conclusions can be drawn from Figure 10. First, the restoration effect of the six restoration results corresponding to the solar wind density from high to low gradually becomes worse. This is because the lower the solar wind number density, the fewer SWCX processes occur in the Earth's magnetopause. This makes for fewer photons detected by the SXI, so fewer features that can be extracted for the recovery network, resulting in a poor recovery effect. Second, the restoration results of the proposed method after smoothing are significantly better than those of other typical image restoration methods. The PSNR of the smoothed restoration results of the proposed method is approximately 30 dB, and the SSIM is approximately 0.8; these values are significantly higher than with the other methods. Hence, the proposed image restoration method is superior to other methods in restoring the SXI photon counting images. In addition, K-SVD performs best among the traditional methods, and the other three methods have similar effects. It is worth mentioning that from the restoration results shown in Figure 9, we can see that the proposed method is superior to other traditional methods in image edge restoration, which is crucial for the subsequent reconstruction of the Earth's magnetopause.

4.3 Tangent Fitting Approach (TFA) Analysis

From 2-D X-ray images, we cannot directly obtain the magnetopause position information and the response of the magnetopause to the change in the solar wind, so it is necessary to obtain more information from the observation image. Several methods have been developed to reconstruct a 3-D magnetopause from such 2-D X-ray images (Wang C and Sun TR, 2022). Among them, Sun TR et al. (2020) proposed the TFA, which reconstructs the 3-D magnetopause from a single X-ray image by finding the best match of the tangential directions. The maximum X-ray intensity corresponds to the tangential direction of the magnetopause (Collier and Connor, 2018). Therefore, the position of the maximum X-ray intensity in 2-D X-ray images is the input of the TFA method and is the key to influencing its output results. We

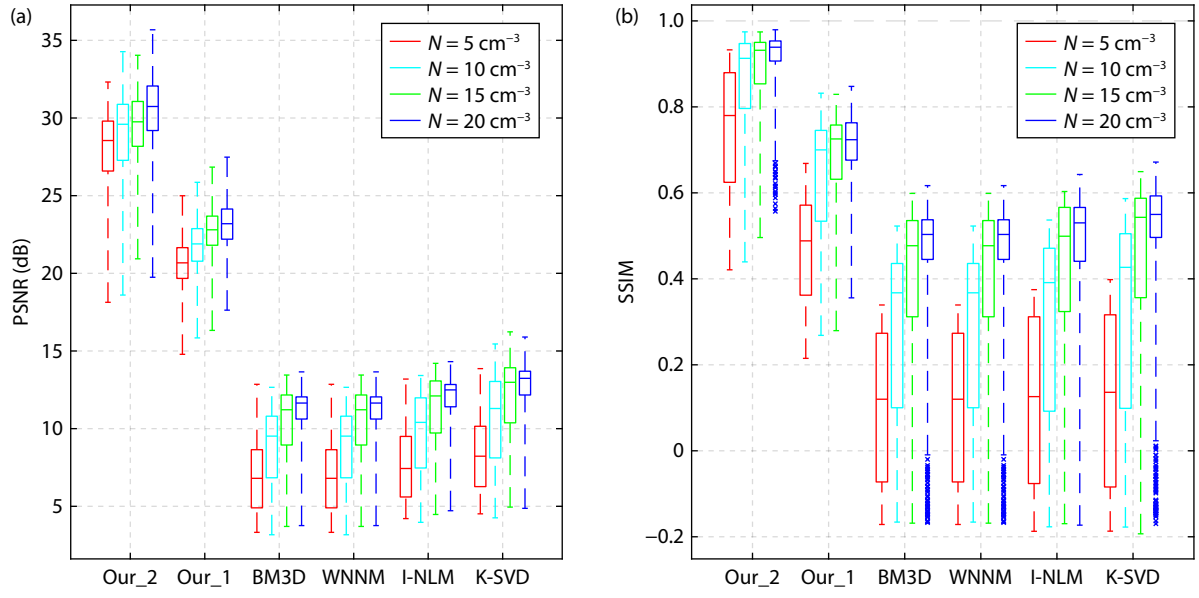

Figure 10. (a) PSNR statistics calculated for six different restoration results with MHD X-ray images; (b) statistical data of the SSIM between MHD X-ray images and the six restoration results. The red, cyan, green, and blue boxes correspond to solar wind densities of $N = 5$ cm^{-3}, $N = 10$ cm^{-3}, $N = 15$ cm^{-3}, and $N = 20$ cm^{-3}, respectively. Other solar wind conditions are $V_x = 600$ km/s and $B_z = 0$ nT. The X-axis labels of BM3D, WNNM, I-NLM, and K-SVD are four different existing recovery methods. Our_1 represents the statistical result before smoothing, as obtained by the proposed restoration algorithm, and Our_2 represents the statistical result after smoothing. The box plot is a standard way of describing the distribution of data by five numbers: minimum, first quantile, median, third quantile, and maximum. The symbol "x" after the dotted line indicates an outlier.

take the position information of the maximum X-ray intensity as an index to evaluate the restoration effect. Figure 11 shows its position in MHD X-ray images, SXI photon count images after adding a constant sky background, and restored images smoothed by this method under four solar wind densities.

Figure 11 shows the positions of the maximum X-ray intensities for different images. The position of N_{SXI} is scattered, and a big gap exists between the position of N_{SXI} and I_{MHD}. The position of N_{Our} is very close to the position of I_{MHD}, which indicates that the restoration result can provide a more accurate input (N_{SXI}) to the TFA method. The root mean square error (RMSE) is often used to evaluate the accuracy of curve fitting. We use it to measure the distance between the position of the maximum X-ray intensity of different images. The RMSE error is defined as

$$\mathrm{RMSE} = \sqrt{\frac{\sum_{i=1}^{N}(y_i - \hat{y}_i)^2}{N}}. \tag{21}$$

Each row has a position with the largest X-ray intensity, so the value of N is 55. Variables y_i and $\hat{y}_i$, respectively, represent the abscissa corresponding to the position of the largest X-ray intensity in the ith row of the two images. The RMSE represents the deviation of data from the true value. Figure 12 shows the RMSE between the locations of maximum X-ray intensity in three images (I_{MHD}, N_{SXI}, and N_{Our}).

Figure 12 compares I_{MHD}, N_{SXI}, and N_{Our} of the MHD X-ray images after adding a constant sky background, the SXI photon count images after adding a constant sky background, and the image restored by the proposed method, from which two conclusions can be drawn. First, the image recovered by the proposed method

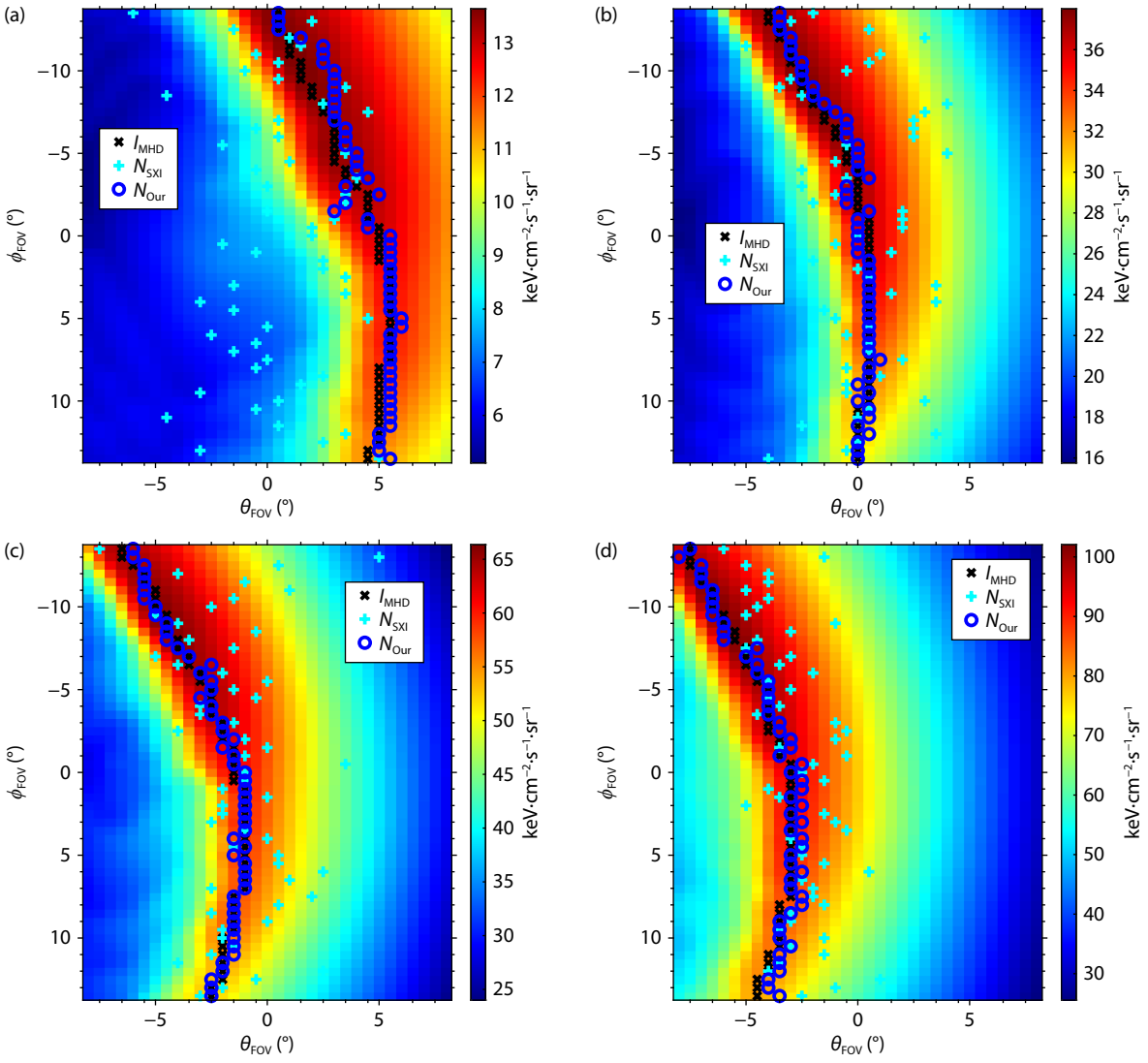

Figure 11. The observation position of (a)–(d) is (–3.8638, 11.6590, 14.7665) R_E, and the SXI aim point is (10.6226, 0.0139, 0) R_E. The black crosses represent the position of maximum value of the MHD X-ray image intensity (I_{MHD}). The cyan plus signs represent the position of the maximum photon count of the SXI photon count images after adding a constant sky background (N_{SXI}). The blue circles mark the position of the maximum X-ray intensity of the restored images after smoothing processes (N_{Our}). The background colors in the figure correspond to MHD X-ray images (with added sky background) with different solar wind number densities. The solar wind number densities of (a) to (d) are N = 5cm^{-3}, N = 10 cm^{-3}, N = 15 cm^{-3}, and N = 20 cm^{-3}, respectively. Other solar wind conditions are V_x = 600 km/s and B_z = 0 nT.

can provide the TFA method with approximately the same position information on the maximum X-ray intensity as the MHD X-ray images, as input. The RMSE between N_{Our} and I_{MHD} is smaller than that between N_{SXI} and I_{MHD}, and the former is very close to zero. This result indicates that the position of the maximum X-ray intensity of the restored image is very close to that of the MHD X-ray images, and its position information can be used directly to reconstruct the 3-D magnetopause at the appropriate observation position. At the same time, not all MHD X-ray images of the observed locations contain the entire magnetopause profile structure, and the TFA method cannot obtain the accurate output from such 2-D X-ray images that do not contain the complete magnetospheric structure. Second, the RMSE fluctuated significantly and showed an increasing trend as the *Z*-coordinate of the observed position decreased. This is caused by the observed locations of the low *Z*-axis coordinates being very close to the magnetopause (Jorgensen et al., 2022; Samsonov et al., 2022), which results in very little information about the locations of the maximum X-ray intensity of the magnetosheath profile observed by the SXI. Hence, the observation area between the two green lines is not suitable for the TFA method, and the observation positions with the lower *Z*-axis coordinates can be ignored. In summary, compared with the SXI photon count images, the images recovered by the proposed method can provide more accurate inputs for the TFA method, resulting in more accurate reconstruction results.

4.4 Computed Tomography Approach (CTA) Reconstruction

The CTA is a traditional computed tomography method applied to magnetospheric X-ray image reconstruction (Sun TR et al., 2020). It relies on a set of 2-D X-ray images and reconstructs the 3-D X-ray emissivity from which the 3-D magnetopause surface can then be derived. The CTA does not depend on the functional form of the magnetopause, bow shock, or X-ray emissivity. However, it requires a group of images for the same magnetopause profile, so it is not applicable to events with rapid changes in the solar wind

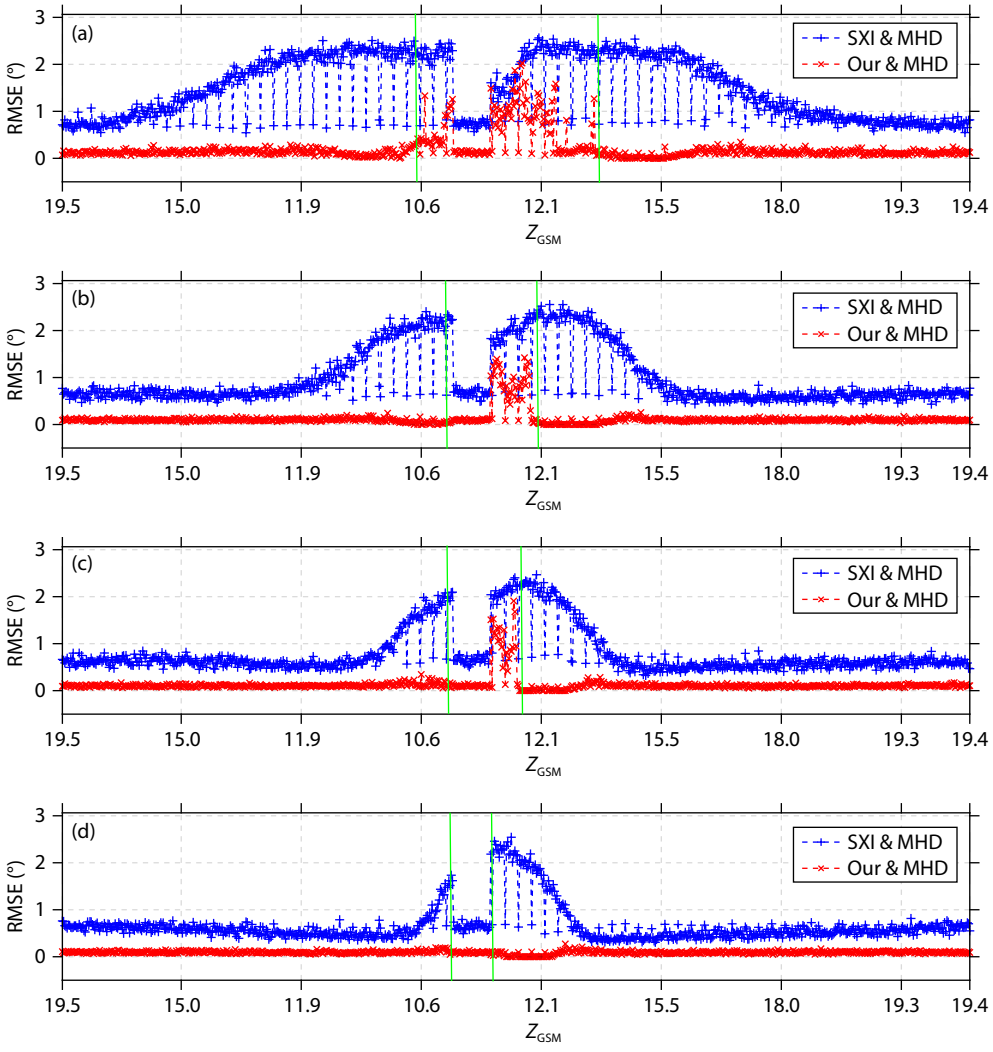

Figure 12. Solar wind number densities of (a)–(d) are N = 5 cm^{-3}, N = 10 cm^{-3}, N = 15 cm^{-3}, and N = 20 cm^{-3}, respectively. The *X*-axis of the broken-line graph is the *Z*-coordinate of the corresponding observation position of 757 images in the GSM coordinate system. The *Y*-axis is the RMSE. The blue lines are the RMSE between N_{SXI} and I_{MHD}. The red lines are the RMSE between N_{Our} and I_{MHD}. The observation area between the two green lines indicates that the SXI is too close to the interior of the magnetopause and that the imaging results of these observation locations cannot be used by the TFA method.

(Jorgensen et al., 2022). Wang RC et al. (2023) proposed the use of artificial intelligence to complete the image of the observation angle that the orbit failed to cover, and to retrieve the 3-D magnetopause configuration to make up for its unsuitability for events with rapid changes in the solar wind. Therefore, the CTA method has become an essential member of the toolbox for the inversion of the 3-D magnetospheric top with 2-D X-ray images (Wang C and Sun TR, 2022).

We use a series of SXI photon count images after adding a constant sky background and the restored image of the proposed method, as obtained from the semicircular orbit mentioned in Section 4.1, and we use these as the inputs of the TFA method to reconstruct the X-ray emissivity of the 3-D Earth magnetopause. The Feldkamp–Davis–Kress algorithm (Feldkamp et al., 1984; Pan XC et al., 2009; Wang RC et al., 2023) is used to reconstruct the X-ray emissivity of the 3-D Earth magnetopause. The original MHD X-ray emissivity and corresponding reconstruction results are shown in Figure 13. We compare the MHD X-ray emissions, SXI reconstruction results, and reconstruction results obtained from the proposed image restoration method under four solar wind conditions.

As described in Section 4.2, we used the PSNR and SSIM to evaluate the reconstruction results. We calculated the reconstruction results of the SXI photon count image after adding a constant sky background and those of the restored image in this work with the corresponding PSNR and SSIM of the original MHD X-ray emissions. The calculation results are shown in Table 3.

As shown in Table 3, the 3-D reconstruction results corresponding to 2-D X-ray images obtained by using the proposed restoration method are significantly better than those obtained by using the SXI photon count images directly after adding a constant sky background. This result shows that the proposed restoration method can provide more accurate 2-D X-ray images as inputs for the CTA method, based on the observed data, thus making the reconstruction results more accurate.

Table 3. The PSNR and SSIM between different reconstruction results.[a]

Evaluation index	PSNR (dB)	SSIM	PSNR (dB)	SSIM	PSNR (dB)	SSIM	PSNR (dB)	SSIM
	N = 5 cm^{-3}		N = 10 cm^{-3}		N = 15 cm^{-3}		N = 20 cm^{-3}	
SXI	10.44	0.0968	11.4411	0.3689	11.8575	0.5681	13.6424	0.6739
Our	22.3632	0.9552	24.0414	0.9468	25.6415	0.9521	26.8953	0.9545

[a]N = Number density.

5. Discussion and Summary

As discussed in Section 2.2, we used a unified sky background to obtain the simulated imaging results of the SXI (Guo YH et al., 2022; Samsonov et al., 2022). However, in the actual observation process, the sky background from different perspectives will change. In the future, if a soft X-ray background obtained by the ROSAT sky survey plan can be used to simulate SXI results under a changed background, it may be closer to the real imaging data returned by SXI during the SMILE operation. Alternatively, the soft X-ray background can be reduced or removed as much as possible from the final imaging result of the magnetosheath; the imaging result contaminated by Poisson noise can then be restored by using the proposed method.

According to the analysis in Section 2.3, when the relevant parameters of the SXI are determined, the model matrix $\boldsymbol{H}$ of the observation process will not change with the change in the observation location and target. Therefore, the use of a deep neural network to learn the model matrix of the observation process based on relevant data of the SXI ground calibration process may provide a new perspective on the processing of real SXI observation data acquired after the SMILE launch.

The simulation results of the SXI in this work were obtained by assuming that the satellite position is fixed within the integral time (300 s). In practice, when a satellite is moving at a low speed near apogee, its motion can be ignored. In addition, as the satellite moves closer to Earth, we must consider how its motion affects the image. Therefore, it is necessary to conduct a transient simulation of SXI imaging results.

The restoration method used in this work involves dividing the whole image into several patches by overlapping block technology and then restoring these patches. This method has three advantages. First, patches of the image have strong similarity, and patches after clustering have the same distribution parameters, which is conducive to training the patch estimator. Second, large-scale paired clean–noise images are difficult to obtain, whereas paired clean–noise patches are more likely to quantitatively meet the training requirements of the deep learning networks. Third, there are no restrictions on the absolute position for patches, which makes the final whole image restoration result more generalized. At the same time, the idea of patch estimation is more consistent with the processing requirements of the actual SXI imaging data, although this idea is not perfect. Because the whole image is split, its overall features are not considered, which is reflected in the restoration results presented in Section 4.2. The edges of the restored images become distorted, and the local resolution is low, which can be attributed to patch combination and splitting. Although we use a smoothing technology to process the restored image, the result is still not satisfactory. Many problems still remain to be studied in the restoration of marginal details. In addition, the proposed method preprocesses the SXI observation images, with the ultimate aim of providing 2-D X-ray images containing more information for the reconstruction of the 3-D magnetopause.

We proposed an image restoration algorithm for the SXI observation images that can recover their large-scale magnetospheric structure information. The reconstructed image provides more effective information for the subsequent reconstruction of the 3-D

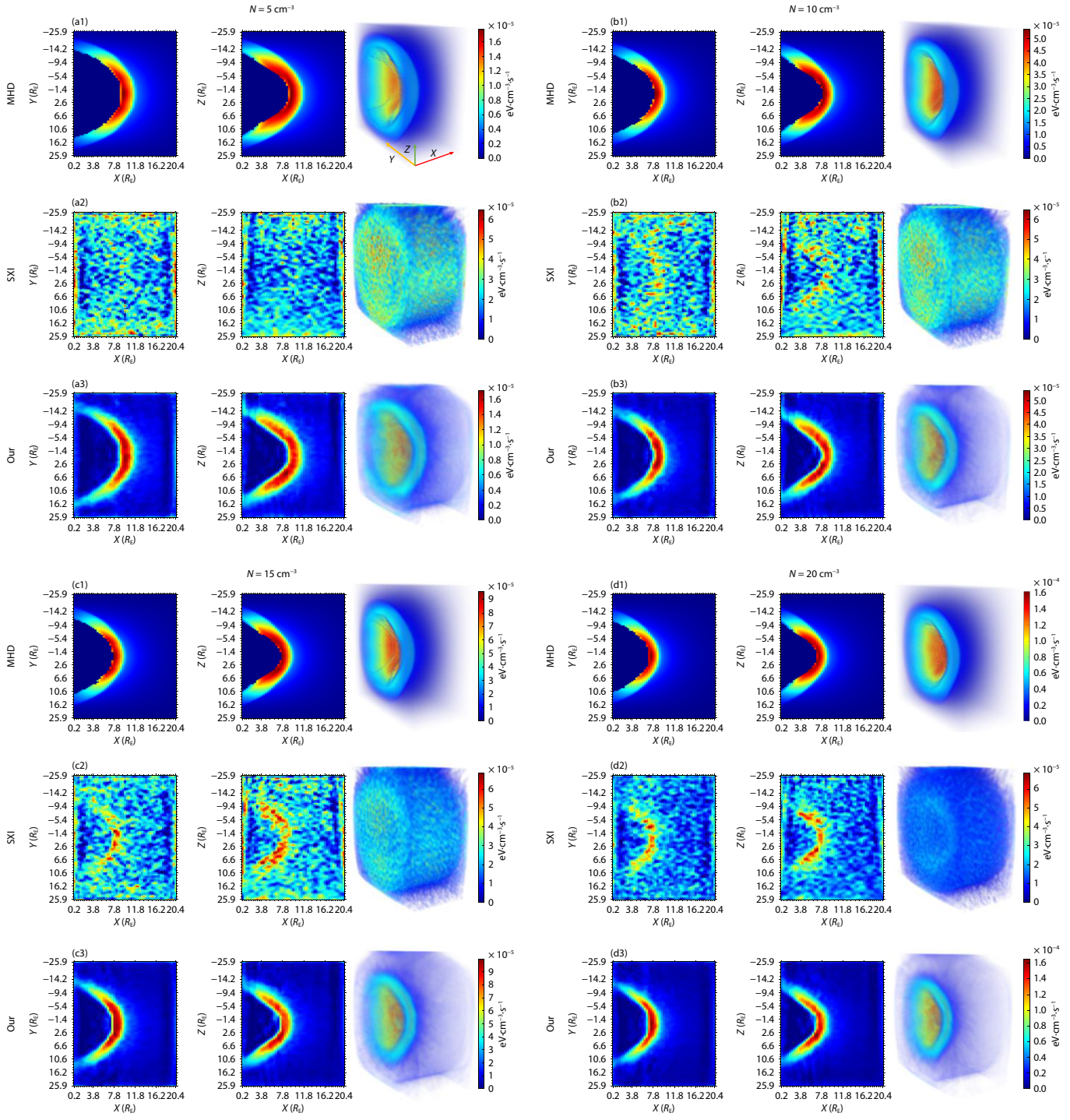

Figure 13. (a1)–(d1) MHD X-ray emissions under four solar wind conditions; (a2)–(d2) reconstruction results of the SXI photon count images after adding a constant sky background; (a3)–(d3) reconstruction results of the proposed image restoration method. Other solar wind conditions are V_x = 600 km/s and B_z = 0 nT.

magnetosheath X-ray emissivity. The image restoration algorithm constructs a dataset of clean–noise patch pairs obtained by an SXI simulation technology, which is the prior knowledge to be learned in the process of image restoration. The CEM algorithm divides the clean–noise patch pair datasets into clusters obeying a multivariate Gaussian distribution. The patches of each cluster are subject to the Gaussian distribution of a set of parameters, which are also used to train the patch estimator of the corresponding cluster. The patch estimator in this work is built based on the pix2pix framework. The estimator can learn the potential mapping relationship between a noise patch and clean patch to achieve the purpose of noise patch estimation. Experiments showed that the proposed image restoration method is superior to other traditional image restoration methods in the effect on SXI observation image restoration. Therefore, the reconstructed image was applied to the TFA and CTA, two 3-D magnetopause

reconstruction algorithms, and both achieved excellent and accurate reconstruction effects. It is worth mentioning that the proposed image restoration algorithm not only is applicable to magnetospheric observation images but also has broad application prospects in the fields of computed tomography and astronomical imaging.

Data Availability Statement

The two groups of orbital coordinates and SXI aim point data used in this research, and all image data used and obtained in the experiments presented in Section 4, can be obtained from the Science Data Bank (https://doi.org/10.57760/sciencedb.07721).

Acknowledgments

This work was supported by the National Natural Science Foundation of China (Grant Nos. 42322408, 42188101, 41974211, and 42074202), the Key Research Program of Frontier Sciences, Chinese Academy of Sciences (Grant No. QYZDJ-SSW-JSC028), and the Strategic Priority Program on Space Science, Chinese Academy of Sciences (Grant Nos. XDA15052500, XDA15350201, and XDA15014800). TianRan Sun was also supported by the Youth Innovation Promotion Association of the Chinese Academy of Sciences (Grant No. Y202045). In addition, we thank LetPub (www.letpub.com) for linguistic assistance during the preparation of this manuscript.

References

Adams, A., Gelfand, N., Dolson, J., and Levoy, M. (2009). Gaussian KD-trees for fast high-dimensional filtering. *ACM Trans. Graph.*, *28*(3), 21. https://doi.org/10.1145/1531326.1531327

Aharon, M., Elad, M., and Bruckstein, A. (2006). K-SVD: An algorithm for designing overcomplete dictionaries for sparse representation. *IEEE Trans. Signal Process.*, *54*(11), 4311–4322. https://doi.org/10.1109/TSP.2006.881199

Barnes, C., Shechtman, E., Dan, B. G., and Finkelstein, A. (2010). The generalized PatchMatch correspondence algorithm. In *11th European Conference on Computer Vision* (pp. 29–43). Heraklion, Crete, Greece: Springer. https://doi.org/10.1007/978-3-642-15558-1_3

Bhardwaj, A., Elsner, R. F., Gladstone, G. R., Cravens, T. E., Lisse, C. M., Dennerl, K., Branduardi-Raymont, G., Wargelin, B. J., Waite, J. H., Jr., … Kharchenko, V. (2007). X-rays from solar system objects. *Planet. Space Sci.*, *55*(9), 1135–1189. https://doi.org/10.1016/j.pss.2006.11.009

Branduardi-Raymont, G., Sembay, S. F., Eastwood, J. P., Sibeck, D. G., Abbey, T. A., Brown, P., Carter, J. A., Carr, C. M., Forsyth, C., … Yeoman, T. K. (2012). AXIOM: Advanced X-ray imaging of the magnetosphere. *Exp. Astron.*, *33*(2-3), 403–443. https://doi.org/10.1007/s10686-011-9239-0

Branduardi-Raymont, G., Escoubet, C. P., Kuntz, K., Lui, T., Read, A., and Sibeck, D. (2016). Link between solar wind, magnetosphere, and ionosphere. *ISSI-BJ Mag., 9*. http://www.issibj.ac.cn/publications/taikong/202201/P020220127540869199726.pdf

Bruzzone, L., and Prieto, D. F. (2001). Unsupervised retraining of a maximum likelihood classifier for the analysis of multitemporal remote sensing images. *IEEE Trans. Geosci. Remote Sens.*, *39*(2), 456–460. https://doi.org/10.1109/36.905255

Buades, A., Coll, B., and Morel, J. M. (2005). A non-local algorithm for image denoising. In *2005 IEEE Computer Society Conference on Computer Vision and Pattern Recognition* (pp. 60–65). San Diego, CA, USA: IEEE. https://doi.org/10.1109/CVPR.2005.38

Buades, T., Lou, Y. F., Morel, J. M., and Tang, Z. W. (2009). A note on multi-image denoising. In *2009 International Workshop on Local and Non-Local Approximation in Image Processing* (pp. 1–15). Tuusula, Finland: IEEE. https://doi.org/10.1109/LNLA.2009.5278408

Carter, J. A., Sembay, S., and Read, A. M. (2010). A high charge state coronal mass ejection seen through solar wind charge exchange emission as detected by *XMM–Newton*. *Mon. Not. Roy. Astron. Soc.*, *402*(2), 867–878. https://doi.org/10.1111/j.1365-2966.2009.15985.x

Celeux, G., and Govaert, G. (1992). A classification EM algorithm for clustering and two stochastic versions. *Comput. Statist. Data Anal.*, *14*(3), 315–332. https://doi.org/10.1016/0167-9473(92)90042-E

Chan, S. H., Zickler, T., and Lu, Y. M. (2014). Monte Carlo non-local means: Random sampling for large-scale image filtering. *IEEE Trans. Image Process.*, *23*(8), 3711–3725. https://doi.org/10.1109/TIP.2014.2327813

Chen, F., Zhang, L., and Yu, H. M. (2015). External patch prior guided internal clustering for image denoising. In *2015 IEEE International Conference on Computer Vision* (pp. 603–611). Santiago, Chile: IEEE. https://doi.org/10.1109/ICCV.2015.76

Collier, M. R., Porter, F. S., Sibeck, D. G., Carter, J. A., Chiao, M. P., Chornay, D., Cravens, T., Galeazzi, M., Keller, J. W., … Thomas, N. (2012). Prototyping a global soft X-ray imaging instrument for heliophysics, planetary science, and astrophysics science. *Astron. Nachr.*, *333*(4), 378–382. https://doi.org/10.1002/asna.201211662

Collier, M. R., and Connor, H. K. (2018). Magnetopause surface reconstruction from tangent vector observations. *J. Geophys. Res.: Space Phys.*, *123*(12), 10189–10199. https://doi.org/10.1029/2018JA025763

Cravens, T. E. (1997). Comet Hyakutake X-ray source: Charge transfer of solar wind heavy ions. *Geophys. Res. Lett.*, *24*(1), 105–108. https://doi.org/10.1029/96GL03780

Cravens, T. E. (2000). Heliospheric X-ray emission associated with charge transfer of the solar wind with interstellar neutrals. *Astrophys. J.*, *532*(2), L153–L156. https://doi.org/10.1086/312574

Cravens, T. E., Robertson, I. P., and Snowden, S. L. (2001). Temporal variations of geocoronal and heliospheric X-ray emission associated with the solar wind interaction with neutrals. *J. Geophys. Res.: Space Phys.*, *106*(A11), 24883–24892. https://doi.org/10.1029/2000JA000461

Dabov, K., Foi, A., Katkovnik, V., and Egiazarian, K. (2007). Image denoising by sparse 3-D transform-domain collaborative filtering. *IEEE Trans. Image Process.*, *16*(8), 2080–2095. https://doi.org/10.1109/TIP.2007.901238

Dempster, A. P., Laird, N. M., and Rubin, D. B. (1977). Maximum likelihood from incomplete data via the EM algorithm. *J. R. Stat. Soc. B Stat. Methodol.*, *39*(1), 1–38.

Dong, W. S., Shi, G., and Li, X. (2013). Nonlocal image restoration with bilateral variance estimation: A low-rank approach. *IEEE Trans. Image Process.*, *22*(2), 700–711. https://doi.org/10.1109/TIP.2012.2221729

Elad, M., and Aharon, M. (2006). Image denoising via sparse and redundant representations over learned dictionaries. *IEEE Trans. Image Process.*, *15*(12), 3736–3745. https://doi.org/10.1109/TIP.2006.881969

Ewald, P. P., Ed. (1962). *50 Years of X-ray Diffraction*. Springer-Verlag US., 978-90-277-9029-3. https://doi.org/10.1007/978-1-4615-9961-6

Feldkamp, L. A., Davis, L. C., and Kress, J. W. (1984). Practical cone-beam algorithm. *J. Opt. Soc. Am. A*, *1*(6), 612–619. https://doi.org/10.1364/JOSAA.1.000612

Ferrara, E. (1980). Fast implementations of LMS adaptive filters. *IEEE Trans. Acoust. Speech Signal Process.*, *28*(4), 474–475. https://doi.org/10.1109/TASSP.1980.1163432

Freeman, W. T., Jones, T. R., and Pasztor, E. C. (2002). Example-based super-resolution. *IEEE Comput. Graph. Appl.*, *22*(2), 56–65. https://doi.org/10.1109/38.988747

Giacconi, R., Gursky, H., Paolini, F. R., and Rossi, B. B. (1962). Evidence for X rays from sources outside the solar system. *Phys. Rev. Lett.*, *9*, 439. https://doi.org/10.1103/PhysRevLett.9.439

Goodfellow, I. J., Pouget-Abadie, J., Mirza, M., Xu, B., Warde-Farley, D., Ozair, S., Courville, A., and Bengio, Y. (2014). Generative adversarial networks. In *Proceedings of the 27th International Conference on Neural Information Processing Systems* (pp. 2672–2680). Montreal, Canada: MIT Press.

Gorenstein, P. (2010). Focusing X-ray optics for astronomy. *X-Ray Opt. Instrum.*, *2010*, 109740. https://doi.org/10.1155/2010/109740

Gu, S. H., Lei, Z., Zuo, W. M., and Feng, X. C. (2014). Weighted nuclear norm minimization with application to image denoising. In *2014 IEEE Conference on Computer Vision and Pattern Recognition* (pp. 2862–2869). Columbus, OH, USA: IEEE. https://doi.org/10.1109/CVPR.2014.366

Gu, S. H., and Timofte, R. (2019). A brief review of image denoising algorithms and beyond. In S. Escalera, et al. (Eds.), *Inpainting and Denoising Challenges* (pp. 1–21). Switzerland: Springer. https://doi.org/10.1007/978-3-030-25614-2_1

Guo, Y. H., Wang, C., Wei, F., Sun, T. R., Yu, X. Z., Peng, S. W., Branduardi-Raymont, G., and Sembay, S. (2021). A Lunar-based Soft X-ray Imager (LSXI) for the Earth's magnetosphere. *Sci. China Earth Sci.*, *64*(7), 1026–1035. https://doi.org/10.1007/s11430-020-9792-5

Guo, Y. H., Sun, T. R., Wang, C., and Sembay, S. (2022). Deriving the magnetopause position from wide field-of-view soft X-ray imager simulation. *Sci. China Earth Sci.*, *65*(8), 1601–1611. https://doi.org/10.1007/s11430-021-9937-y

Hays, J., and Efros, A. A. (2007). Scene completion using millions of photographs. *ACM Trans. Graph.*, Volume 26, Issue 3, pp 4–es.. https://doi.org/10.1145/1276377.1276382

He, K. M., and Sun, J. (2012). Computing nearest-neighbor fields via propagation-assisted KD-trees. In *2012 IEEE Conference on Computer Vision and Pattern Recognition* (pp. 111–118). Providence, RI, USA: IEEE. https://doi.org/10.1109/CVPR.2012.6247665

Hodges, R. R. Jr. (1994). Monte Carlo simulation of the terrestrial hydrogen exosphere. *J. Geophys. Res.: Space Phys.*, *99*(A12), 23229–23247. https://doi.org/10.1029/94JA02183

Hu, Y. Q., Guo, X. C., and Wang, C. (2007). On the ionospheric and reconnection potentials of the Earth: Results from global MHD simulations. *J. Geophys. Res.: Space Phys.*, *112*(A7), A07215. https://doi.org/10.1029/2006JA012145

Isola, P., Zhu, J. Y., Zhou, T. H., and Efros, A. A. (2017). Image-to-image translation with conditional adversarial networks. In *2017 IEEE Conference on Computer Vision and Pattern Recognition* (pp. 5967–5976). Honolulu, HI, USA: IEEE. https://doi.org/10.1109/CVPR.2017.632

Jorgensen, A. M., Sun, T. R., Wang, C., Dai, L., Sembay, S., Wei, F., Guo, Y. H., and Xu, R. L. (2019a). Boundary detection in three dimensions with application to the SMILE mission: The effect of photon noise. *J. Geophys. Res.: Space Phys.*, *124*(6), 4365–4383. https://doi.org/10.1029/2018JA025919

Jorgensen, A. M., Sun, T. R., Wang, C., Dai, L., Sembay, S., Zheng, J. H., and Yu, X. Z. (2019b). Boundary detection in three dimensions with application to the SMILE mission: The effect of model-fitting noise. *J. Geophys. Res.: Space Phys.*, *124*(6), 4341–4355. https://doi.org/10.1029/2018JA026124

Jorgensen, A. M., Xu, R., Sun, T., Huang, Y., Li, L., Dai, L., and Wang, C. (2022). A theoretical study of the tomographic reconstruction of magnetosheath X-ray emissions. *J. Geophys. Res.: Space Phys.*, *127*(4), e2021JA029948. https://doi.org/10.1029/2021JA029948

Kersten, P. R., Lee, J. S., and Ainsworth, T. L. (2005). Unsupervised classification of polarimetric synthetic aperture radar images using fuzzy clustering and EM clustering. *IEEE Trans. Geosci. Remote Sens.*, *43*(3), 519–527. https://doi.org/10.1109/TGRS.2004.842108

Kingma, D., and Ba, J. (2017). Adam: A method for stochastic optimization. arXiv:1412.6980. https://doi.org/10.48550/arXiv.1412.6980

Krizhevsky, A., Sutskever, I., and Hinton, G. E. (2012). ImageNet classification with deep convolutional neural networks. In *Proceedings of the 25th International Conference on Neural Information Processing Systems* (pp. 1097–1105). Lake Tahoe, NV, USA: Curran Associates Inc.

Lebrun, M. (2012). An analysis and implementation of the BM3D image denoising method. *Image Process. Line*, *2*, 175–213. https://doi.org/10.5201/ipol.2012.l-bm3d

Levin, A., and Nadler, B. (2011). Natural image denoising: Optimality and inherent bounds. In *CVPR 2011* (pp. 2833–2840). Colorado Springs, CO, USA: IEEE. https://doi.org/10.1109/CVPR.2011.5995309

Levin, A., Nadler, B., Durand, F., and Freeman, W. T. (2012). Patch complexity, finite pixel correlations and optimal denoising. In *13th European Conference on Computer Vision* (pp. 73–86). Florence, Italy: Springer. https://doi.org/10.1007/978-3-642-33715-4_6

Liou, C. Y., Huang, J. C., and Yang, W. C. (2008). Modeling word perception using the Elman network. *Neurocomputing*, *71*(16-18), 3150–3157. https://doi.org/10.1016/j.neucom.2008.04.030

Liou, C. Y., Cheng, W. C., Liou, J. W., and Liou, D. R. (2014). Autoencoder for words. *Neurocomputing*, *139*, 84–96. https://doi.org/10.1016/j.neucom.2013.09.055

Lisse, C. M., Dennerl, K., Englhauser, J., Harden, M., Marshall, F. E., Mumma, M. J., Petre, R., Pye, J. P., Ricketts, M. J., … West, R. G. (1996). Discovery of X-ray and extreme ultraviolet emission from comet C/Hyakutake 1996 B2. *Science*, *274*(5285), 205–209. https://doi.org/10.1126/science.274.5285.205

Luo, E. M., Chan, S. H., and Nguyen, T. Q. (2015). Adaptive image denoising by targeted databases. *IEEE Trans. Image Process.*, *24*(7), 2167–2181. https://doi.org/10.1109/TIP.2015.2414873

McLachlan, G., and Peel, D. (2000). *Finite Mixture Models*. New York: John Wiley & Sons, Inc. http://dx.doi.org/10.1002/0471721182

Mirza, M., and Osindero, S. (2014). Conditional generative adversarial nets. arXiv:1411.1784. https://doi.org/10.48550/arXiv.1411.1784

Mosseri, I., Zontak, M., and Irani, M. (2013). Combining the power of Internal and External denoising. In *IEEE International Conference on Computational Photography* (pp. 1–9). Cambridge, MA, USA: IEEE. https://doi.org/10.1109/ICCPhot.2013.6528298

Nash, J. F. (1950). Equilibrium points in *N*-person games. *Proc. Natl. Acad. Sci. USA*, *36*(1), 48–49. https://doi.org/10.1073/pnas.36.1.48

Niknejad, M., Rabbani, H., and Babaie-Zadeh, M. (2015). Image restoration using Gaussian mixture models with spatially constrained patch clustering. *IEEE Trans. Image Process.*, *24*(11), 3624–3636. https://doi.org/10.1109/TIP.2015.2447836

Niknejad, M., Bioucas-Dias, J., and Figueiredo, M. A. T. (2019). External patch-based image restoration using importance sampling. *IEEE Trans. Image Process.*, *28*(9), 4460–4470. https://doi.org/10.1109/TIP.2019.2912122

Pan, X. C., Sidky, E. Y., and Vannier, M. (2009). Why do commercial CT scanners still employ traditional, filtered back-projection for image reconstruction?. *Inverse Problems*, *25*(12), 123009. https://doi.org/10.1088/0266-5611/25/12/123009

Paszke, A., Gross, S., Massa, F., Lerer, A., Bradbury, J., Chanan, G., Killeen, T., Lin, Z. M., Gimelshein, N., … Chintala, S. (2019). PyTorch: An imperative style, high-performance deep learning library. arXiv:1912.01703. https://doi.org/10.48550/arXiv.1912.01703

Pathak, D., Krähenbuhl, P., Donahue, J., Darrell, T., and Efros, A. A. (2016). Context encoders: Feature learning by inpainting. In *2016 IEEE Conference on Computer Vision and Pattern Recognition* (pp. 2536–2544). Las Vegas, NV, USA: IEEE. https://doi.org/10.1109/CVPR.2016.278

Peele, A. G., Lyngsjo, H., Crocker, R. M., Markham, J., Bannister, N., and Nugent, K. A. (2004). Modeling of the Lobster-ISS X-ray telescope in orbit. In *Proceedings Volume 5488, UV and Gamma-Ray Space Telescope Systems* (pp. 232–241). Glasgow, United Kingdom: SPIE. https://doi.org/10.1117/12.550975

Peng, S. W., Ye, Y. Z., Wei, F., Yang, Z. H., Guo, Y. H., and Sun, T. R. (2018). Numerical model built for the simulation of the earth magnetopause by lobster-eye-type soft X-ray imager onboard SMILE satellite. *Opt. Express*, *26*(12), 15138–15152. https://doi.org/10.1364/OE.26.015138

Radford, A., Metz, L., and Chintala, S. (2016). Unsupervised representation learning with deep convolutional generative adversarial networks. arXiv:1511.06434. https://doi.org/10.48550/arXiv.1511.06434

Ronneberger, O., Fischer, P., and Brox, T. (2015). U-Net: Convolutional networks for biomedical image segmentation. In *18th International Conference on Medical Image Computing and Computer-Assisted Intervention* (pp. 234–241). Munich, Germany: Springer. https://doi.org/10.1007/978-3-319-24574-4_28

Röntgen, W. C. (1896). On a new kind of rays. *Nature*, 53, 274–276. https://doi.org/10.1038/053274b0

Sabol, E. J., and Snowden, S L. (2019). sxrbg: ROSAT X-ray background tool. Astrophysics Source Code Library. ascl: 1904.001. https://ui.adsabs.harvard.edu/abs/2019ascl.soft04001S

Salimans, T., Goodfellow, I., Zaremba, W., Cheung, V., Radford, A., and Chen, X. (2016). Improved techniques for training GANs. arXiv:1606.03498. https://doi.org/10.48550/arXiv.1606.03498

Samsonov, A., Sembay, S., Read, A., Carter, J. A., Branduardi-Raymont, G., Sibeck,

D., and Escoubet, P. (2022). Finding magnetopause standoff distance using a Soft X-ray Imager: 2. Methods to analyze 2-D X-ray images. *J. Geophys. Res.: Space Phys.*, *127*(12), e2022JA030850. https://doi.org/10.1029/2022JA030850

Shelhamer, E., Long, J., and Darrell, T. (2017). Fully convolutional networks for semantic segmentation. *IEEE Trans. Pattern Anal. Mach. Intell.*, *39*(4), 640–651. https://doi.org/10.1109/TPAMI.2016.2572683

Shue, J. H., Chao, J. K., Fu, H. C., Russell, C. T., Song, P., Khurana, K. K., and Singer, H. J. (1997). A new functional form to study the solar wind control of the magnetopause size and shape. *J. Geophys. Res.: Space Phys.*, *102*(A5), 9497–9511. https://doi.org/10.1029/97JA00196

Sibeck, D. G., Allen, R., Aryan, H., Bodewits, D., Brandt, P., Branduardi-Raymont, G., Brown, G., Carter, J. A., Collado-Vega, Y. M., … Wing, S. (2018). Imaging plasma density structures in the soft X-rays generated by solar wind charge exchange with neutrals. *Space Sci. Rev.*, *214*(4), 79. https://doi.org/10.1007/s11214-018-0504-7

Snowden, S. L., Collier, M. R., Cravens, T., Kuntz, K. D., Lepri, S. T., Robertson, I., and Tomas, L. (2009). Observation of solar wind charge exchange emission from exospheric material in and outside Earth's magnetosheath 2008 September 25. *Astrophys. J.*, *691*(1), 372. https://doi.org/10.1088/0004-637X/691/1/372

Sun, T. R., Wang, C., Wei, F., and Sembay, S. (2015). X-ray imaging of Kelvin–Helmholtz waves at the magnetopause. *J. Geophys. Res.: Space Phys.*, *120*(1), 266–275. https://doi.org/10.1002/2014JA020497

Sun, T. R., Wang, C., Sembay, S. F., Lopez, R. E., Escoubet, C. P., Branduardi-Raymont, G., Zheng, J. H., Yu, X. Z., Guo, X. C., … Guo, Y. H. (2019). Soft X-ray imaging of the magnetosheath and cusps under different solar wind conditions: MHD simulations. *J. Geophys. Res.: Space Phys.*, *124*(4), 2435–2450. https://doi.org/10.1029/2018JA026093

Sun, T. R., Wang, C., Connor, H. K., Jorgensen, A. M., and Sembay, S. (2020). Deriving the magnetopause position from the soft X-ray image by using the tangent fitting approach. *J. Geophys. Res.: Space Phys.*, *125*(9), e2020JA028169. https://doi.org/10.1029/2020JA028169

Tadjudin, S., and Landgrebe, D. A. (1996). A decision tree classifier design for high-dimensional data with limited training samples. In *International Geoscience & Remote Sensing Symposium* (pp. 790–792). Lincoln, NE, USA: IEEE. https://doi.org/10.1109/IGARSS.1996.516476

Teodoro, A., Almeida, M., and Figueiredo, M. (2015). Single-frame image denoising and inpainting using Gaussian mixtures. In *Proceedings of the International Conference on Pattern Recognition Applications and Methods* (pp. 283–288). Lisbon, Portugal: Science and Technology Publications. https://doi.org/10.5220/0005256502830288

Tucker, W., and Giacconi, R. (1985). *The X-ray Universe*. Cambridge, MA, USA: Harvard University Press.

Walsh, B. M., Niehof, J., Collier, M. R., Welling, D. T., Sibeck, D. G., Mozer, F. S., Fritz, T. A., and Kuntz, K. D. (2016). Density variations in the Earth's magnetospheric cusps. *J. Geophys. Res.: Space Phys.*, *121*(3), 2131–2142. https://doi.org/10.1002/2015JA022095

Wang, C., Li, Z. J., Sun, T. R., Liu, Z. Q., Liu, J., Wu, Q., Zheng, J. H., and Li, J. (2017). SMILE satellite mission survey. *Space Int.*, *8*, 13–16 (in Chinese). https://doi.org/10.3969/j.issn.1009-2366.2017.08.003

Wang, C., and Sun, T. R. (2022). Methods to derive the magnetopause from soft X-ray images by the SMILE mission. *Geosci. Lett.*, *9*(1), 30. https://doi.org/10.1186/S40562-022-00240-Z

Wang, R. C., Li, D. L., Sun, T. R., Peng, X. D., Yang, Z., and Wang, J. Q. (2023). A 3D magnetospheric CT reconstruction method based on 3D GAN and supplementary limited-angle 2D soft X-ray images. *J. Geophys. Res.: Space Phys.*, *128*(1), e2022JA030424. https://doi.org/10.1029/2022JA030424

Yan, R. M., Shao, L., Liu, L., and Liu, Y. (2014). Natural image denoising using evolved local adaptive filters. *Signal Process.*, *103*, 36–44. https://doi.org/10.1016/j.sigpro.2013.11.019

Zontak, M., and Irani, M. (2011). Internal statistics of a single natural image. In *CVPR 2011* (pp. 977–984). Colorado Springs, CO, USA: IEEE. https://doi.org/10.1109/CVPR.2011.5995401

Zoran, D., and Weiss, Y. (2011). From learning models of natural image patches to whole image restoration. In *2011 International Conference on Computer Vision* (pp. 479–486). Barcelona, Spain: IEEE. https://doi.org/10.1109/ICCV.2011.6126278